UCLA
UCLA Previously Published Works

Title

Template-Free Scalable Fabrication of Linearly Periodic Microstructures by Controlling Ribbing Defects Phenomenon in Forward Roll Coating for Multifunctional Applications

Permalink

https://escholarship.org/uc/item/4bm880sw

Journal

Advanced Materials Interfaces, 9(27)

ISSN

2196-7350

Authors

Islam, Didarul
Perera, Himendra
Black, Benjamin
et al.

Publication Date

2022-09-01

DOI

10.1002/admi.202201237

Peer reviewed

Template-Free Scalable Fabrication of Linearly Periodic Microstructures by Controlling Ribbing Defects Phenomenon in Forward Roll Coating for Multifunctional Applications

Md Didarul Islam, Himendra Perera, Benjamin Black, Matthew Phillips, Muh-Jang Chen, Greyson Hodges, Allyce Jackman, Yuxuan Liu, Chang-Jin Kim, Mohammed Zikry, Saad Khan, Yong Zhu, Mark Pankow, and Jong Eun Ryu*

Periodic micro/nanoscale structures from nature have inspired the scientific community to adopt surface design for various applications, including superhydrophobic drag reduction. One primary concern of practical applications of such periodic microstructures remains the scalability of conventional microfabrication technologies. This study demonstrates a simple template-free scalable manufacturing technique to fabricate periodic microstructures by controlling the ribbing defects in the forward roll coating. Viscoelastic composite coating materials are designed for roll-coating using carbon nanotubes (CNT) and polydimethylsiloxane (PDMS), which helps achieve a controllable ribbing with a periodicity of 114–700 μm. Depending on the process parameters, the patterned microstructures transition from the linear alignment to a random structure. The periodic microstructure enables hydrophobicity as the water contact angles of the samples ranged from 128° to 158°. When towed in a static water pool, a model boat coated with the microstructure film shows 7%–8% faster speed than the boat with a flat PDMS film. The CNT addition shows both mechanical and electrical properties improvement. In a mechanical scratch test, the cohesive failure of the CNT-PDMS film occurs in ≈90% higher force than bare PDMS. Moreover, the nonconductive bare PDMS shows sheet resistance of 747.84–22.66 Ω $\square^{-1}$ with 0.5 to 2.5 wt% CNT inclusion.

1. Introduction

Biological systems have been utilizing micro/nanoscale structures for millions of years to achieve multifunctional capabilities.[9–11] Nature remains a significant source of inspiration for developing multifunctional surfaces with unique capabilities, including superhydrophobicity,[1,2] self-cleaning,[3,4] anti-icing,[3,5] anti-biofoulin,[6,7] biological sensors,[6] and radiative cooling.[6,8] For example, Namib Desert beetles use the superhydrophobic–superhydrophilic micropatterned skin to harvest water from fog.[12–14] Plants such as lotus utilize microstructures on leaves to influence wetting behavior and enable self-cleaning.[12,15] Sharks' unique skin morphology augments the near-wall vorticity during turbulent flow. This augmentation reduces the skin friction and enables sharks to be one of the most efficient swimming species in the ocean.[16–18] These drag-reducing microstructures are particularly interesting to the scientific community. Thus, researchers have focused on periodic microstructures aligned in the flow direction, similar to sharkskin.[19] In prior modeling and experimentation, researchers have decreased frictional drag by using different variations of linear periodic microstructures. For example, Xu et al. developed a series of linear microtrenches demonstrating a maximum drag reduction of ≈30% in high Reynolds number applications.[20] In addition, Park et al. studied the impact of grating parameters on drag reduction and demonstrated a max drag reduction of 75%.[21]

Lithography is one of the standard processes for manufacturing superhydrophobic periodic microstructures.[20–22]

M. D. Islam, B. Black, M. Phillips, M.-J. Chen, G. Hodges, Y. Liu,
M. Zikry, Y. Zhu, M. Pankow, J. E. Ryu
Department of Mechanical and Aerospace Engineering
NC State University
Raleigh, NC 27695, USA
E-mail: jryu@ncsu.edu

The ORCID identification number(s) for the author(s) of this article can be found under https://doi.org/10.1002/admi.202201237.

H. Perera, S. Khan
Department of Chemical and Biomolecular Engineering
NC State University
Raleigh, NC 27695, USA

A. Jackman
Flow Science Inc.
683 Harkle Road, Santa Fe, NM 87505, USA

C.-J. Kim
Micro and Nano Manufacturing Lab
UCLA Samueli School of Engineering
7400 Boelter Hall, Los Angeles, CA 90095, USA

However, one primary limitation of this method is that the size of the SHPo surface is limited by the substrate size, which in the case of a silicon substrate, ranges from 10 to 30 cm. This is far smaller than actual boats that are larger in magnitude ranging from several meters to hundreds of meters. Thus, the photolithography process is impractical to manufacture large-area substrates due to its high cost and low throughput. Nanoimprint lithography is another technique that can replicate the hydrophobic micropatterns by utilizing flexible polydimethylsiloxane (PDMS). Such a technique has been utilized to mimic lotus leaf microstructure on a surface.[23] Although a high water contact angle was achieved, the method cannot still be utilized on a large scale. Other related technologies such as microcoining, biopattern imprinting, laser cutting, and 3D printing also have critical limitations as these methods are time-consuming, expensive, and complex, compromising the scalability.[24–28] Therefore, creating a scalable manufacturing process to produce SHPo micrograting structures is necessary for practical drag reduction applications.

The challenge of scalable manufacturing of microtrench structures has motivated the authors to look more into a common roll-to-roll manufacturing defect known as ribbing (Figure S1, Supporting Information), where spatially periodic patterns appear transverse to the roll-coating direction.[32–35] During the roll-coating process, a positive pressure gradient is developed in the downstream meniscus of the coating fluid.[36] The flow becomes unstable when the pressure gradient exceeds a critical value, and a finger-like growth is observed.[37,38] The ribbing instability is undesirable in general roll-coating applications, such as painting,[39,40] polymer thin films,[41,42] and flexography printing.[43,44] However, carefully controlling these ribbing patterns could assist in replicating periodic microstructures obtained by the traditional methods.

The ribbing behavior of Newtonian and non-Newtonian fluids has been studied through experimental and computational models to minimize roll-coating defects.[32–35,45] It was found that the ribbing periodicity or wavelength ($\lambda_{Ribbing}$) and amplitude have a strong relationship with material properties as well as process parameters, including the surface energy γ, viscosity η, roller radius R, roller gap d, and roller speed U.[37,38,46,47] For a Newtonian fluid, the onset condition of the ribbing instability was found describable by two dimensionless parameters: the capillary number $Ca = \eta*U/\gamma$ and the geometric factor R/d. The critical capillary number $Ca*$ showed a linear proportionality with the geometric factor R/d for Newtonian fluids.[32,33,35,38,48,49] On the other hand, the critical Capillary number for non-Newtonian fluids is much lower than for Newtonian fluids.[49] However, unlike the Newtonian fluid, the theoretical prediction of the $Ca*$ in the viscoelastic fluid is not obtainable. There remains a lack of understanding of how the ribbing occurs in coating applications. López et al. controlled the elasticity with the concentration of polymer molecules in a Newtonian fluid (glycerol/water) and showed similar trends in the $Ca*$ and the normal stress parallel to the flow as the polymer concentration increases.[49] The results imply that the behavior of the viscoelastic fluid increases the stress in the flow direction by restricting the flow and causes the ribbing instability at a slower roller speed, i.e., a lower capillary number. According to computational simulations, Zevallos et al. showed

that at any given Ca, there is a critical Weissenberg number Wi above which the flow becomes unstable.[36] Most research on non-Newtonian fluids has focused on identifying the critical capillary numbers or threshold conditions to initiate the instabilities. However, the fluid propagation and ribbing formation beyond the onset conditions are yet to be explored.[34,50,51]

An in-depth investigation of the physical properties of the roll-coating pastes and how it influences the ribbing instabilities in a roll-coating process can achieve scalable manufacturing of periodic micropatterns surface. Unlike the roll-coating applications, this study focuses on investigating beyond the onset conditions and carefully controlling the process parameters to manufacture periodic microstructures by controlling the instabilities. One phenomenon observed for most coating materials is that ribbing patterns tend to flatten when the roller stops, as the surface tension dominates over viscosity. However, retaining the deformed shape when the rollers stop is necessary to manufacture periodic microstructures. The surface flattening can be avoided by tailoring the coating liquid's viscoelastic properties. One method to engineer the viscoelasticity of the polymers is nanoparticle addition.[52–54] The desired materials will behave only like a fluid above the yield stress but act solid when the stress is unloaded. Previous studies suggest that the inclusions' volume fraction and geometry influence the composite's rheological properties. Notably, composites with cylindrical or high aspect ratio nanoparticles are more likely to possess yield stress than spherical particles.[55,56]

In this study, an in-depth investigation of the roll-coating parameters to manufacture linear periodic microstructures is conducted. First, the ribbing formation of polydimethylsiloxane (PDMS, Sylgard 184) in a forward roll coating for various process parameters was investigated. The finger-like ribbing was observed during the roll coating. However, when the rollers stopped, the liquid surface flattened due to the surface tension. Thus, a viscoelastic composite paste was formulated by adding cylindrical nanoparticles (carbon nanotubes, CNTs) to PDMS. This helped to achieve a yield behavior and avoid surface tension-driven flattening. Finally, utilizing the composite paste, linearly periodic microstructures were manufactured by the roll-coating process. The physical properties of the coating paste and computational fluid dynamics (CFD) analysis of the roll-coating parameters helped to successfully manipulate the ribbing instabilities to manufacture periodic microstructures. The manufactured samples were then applied to a miniature boat to measure the drag reduction and load testing. In addition, the mechanical and electrical properties of the CNT-PDMS composite were also evaluated for multifunctionality and robustness.

2. Results

2.1. Physical Properties of the PDMS and CNT-PDMS

2.1.1. Rheological Properties

The viscoelastic properties of the coating pastes are investigated first, which were later utilized in CFD analysis and helped determine the desirable properties of the coating paste. **Figure 1**a shows the complex viscosity of the PDMS-only sample as a
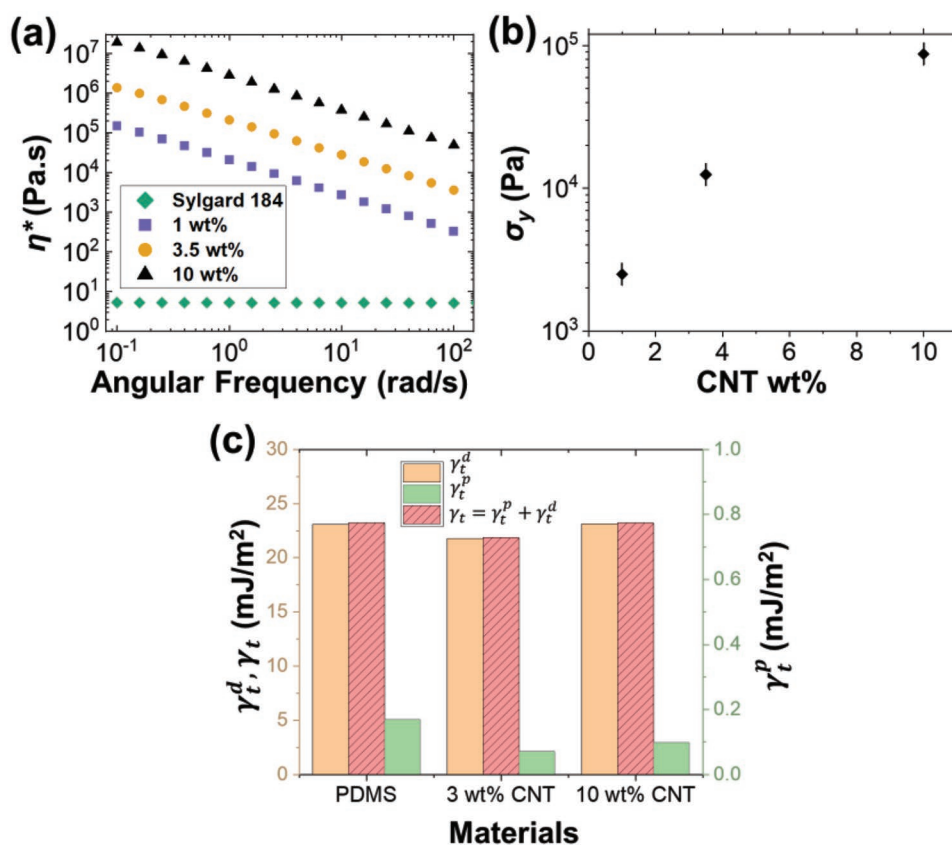
Figure 1. a) Complex viscosity (η^*) versus angular frequency. b) Yield stresses (σ_y) of the composites versus CNT wt%. c) The surface energy components of the materials are based on the fitting.

function of frequency. We find the sample to be Newtonian with a low viscosity consistent with a low molecular weight polymer.[57] The elastic (G') and viscous modulus (G'') also reveal a frequency-dependent behavior with G'' dominating G' indicative of viscoelastic material (Figure S2, Supporting Information). When CNTs are incorporated into the PDMS, both the elastic and viscous moduli increase by several orders of magnitude (Figure S2, Supporting Information). The elastic modulus becomes larger than the viscous modulus, and both are independent of frequency, characteristic of 3D sample spanning networks.[58,59] Such microstructure formation via physical interlocking between the CNTs and PDMS has been suggested before, suppressing the molecular motions of the polymer chains.[60,61] The CNTs entanglement in PDMS is also observed in Figure S3 (Supporting Information).

In Figure 1a, we note that the complex viscosity of the CNT-loaded samples exhibits a power-law behavior with respect to frequency. The absence of a Newtonian regime is consistent with microstructure formation.[62] All samples show a significantly enhanced value compared to PDMS alone; more importantly, we observe a slope approximating −1, suggestive of the presence of yield stress. Huang et al. measured similar trends in this type of system, with high modulus and yield stress values attributed to nanotube clusters which jam and cause internal percolation within the polymer matrix.[63]

In addition to the moduli increase, the physical interlocking of the CNT in the PDMS matrix results in yield stress, which

increases with CNT loading, as seen in Figure 1b. We have used the elastic stress approach to measure the yield stress in this plot.[59,64] The yield stress prevents the paste from flowing until specific stress is met, beneficial as surface features can be preserved postprocessing. This was also confirmed in the subsequent experiment that PDMS could not retain the ribbing shape due to lack of yield behavior, whereas CNT-PDMS samples prevent surface-tension-driven flattening.

2.1.2. Apparent Surface Energy

As discussed prior, the dynamics between surface energy and viscosity of the fluid, often described as a capillary number in roll coating, have a crucial role in ribbing instability. The surface energy (γ) of PDMS has been well-studied.[65–68] The dispersive component of surface energy was measured 17.5–21.7 mJ m^{-2} by several methods such as pendant drop, polymer melt, and liquid contact angle measurements approach.[65–68] The polar component was negligible compared to the dispersive component, as the value ranged from 0.8 to 2.3 mJ m^{-2}. The surface energy of multiwall CNTs was also measured by the Washburn, Wilhelmy, and scanning electron microscopy (SEM) contact angle measurements method.[69–72] The dispersive component of the surface energy of CNTs with 90%–99% purity was 23–37 mJ m^{-2}, whereas the polar part was 0–16.1 mJ m^{-2}.[69–72] Despite the availability of references with PDMS and CNTs surface energy data,

**ADVANCED
SCIENCE NEWS**

www.advancedsciencenews.com

**ADVANCED
MATERIALS
INTERFACES**

www.advmatinterfaces.de

the CNT-PDMS composite has not been studied previously. In this study, three reference liquids, water, diiodomethane (DIM), and ethylene glycol (EG), are used to measure contact angles in several flat samples of the composite materials. The mean and standard deviation (SD) of the measured contact angles are presented in Table S1 (Supporting Information). The data were fitted in Owens–Wendt model [Equations (1) and (2)], and the apparent surface energy was evaluated (Table S1 and Figure S4, Supporting Information). The summary of the apparent surface energy is shown in Figure 1c. The addition of CNTs showed minimal impact on the surface energy of the PDMS. The polar component (γ_t^p) for each test material was low, 0.07–0.17 mJ m^{-2}, and the dispersive component (γ_t^d) was dominant in all cases. The total surface energy (γ_t) for PDMS, 3 wt% CNT, and 10 wt% CNT, was found 23.23, 21.85, and 23.2 mJ m^{-2} based on the Owens–Wendt model. The surface energy of the PDMS was found to be in good agreement with the prior studies validating the experimental method. The results provide further understanding for the next phase of this study. As the surface energy of the composite appears to be dominant by the PDMS, the only scope to tune to dynamics between viscous force and surface energy would rely on tuning the viscoelastic properties as observed in the prior section.

2.2. Ribbing Instabilities in Roll-Coating

2.2.1. CFD Simulation of Roll-Coating of PDMS

A fundamental limitation in all prior studies related to roll-coating of non-Newtonian materials was defining the process parameters during the roll coating, such as the capillary number Ca^*, shear rate $(\dot{\gamma})$, and wall shear stress (τ_w). The shear rate-dependent viscoelastic behavior of the coating materials is usually obtained by a rheometer. However, the roll-coating instruments are not intrinsically viscometric, as they do not have the necessary sensors. Thus, the exact viscosity of the coating paste during the roll-coating process is

unknown as the associated shear rate is also unknown. Estimating the capillary number relies on either assuming a constant viscosity or estimating the shear rate based on the velocity of the rollers,[73] which results in inaccurate Ca. Accurate measurement of the shear rate can be obtained by finite element analysis to determine the fluid velocity profile gradient during the roll-coating process.[74,75]

Hence, a CFD simulation was conducted to develop an effective method to determine the unknown process parameters, including the pressure gradient in the fluid flow direction (dp/dx), fluid flow velocities (V_x), shear rate $(\dot{\gamma})$, and wall shear stress (τ_w). These parameters were later studied along with the experimental results for further understanding. A commercial software *FLOW-3D* is utilized to investigate the effect of roll-coating speeds (U) and rollers distance (d) to the parameters mentioned above. Both rollers were kept at the same speed for each simulation $(U_1 = U_2)$.

The ribbing formation was observed in the CFD simulation of roll-coating under various process conditions, as observed in **Figure 2**a. First, a 3D simulation was conducted at a fixed roller speed of $U = 40$ rad s^{-1} for different roller distances (d). A dimensionless parameter (R/d) was defined, where R is the roller radius. The ribbing wavelength $(\lambda_{Ribbing})$ is initially observed to be equally spaced for each condition and reduces from 7.9 to 3.3 mm as R/d increases from 63.5 to 84.67. However, as the R/d further increases to 101.6, the periodicity becomes irregular as $\lambda_{Ribbing}$ observed between 1.6 and 2.5 mm. Finally, with an R/d of 127, the ribbing patterns show further distortion and $\lambda_{Ribbing}$ increases to 5 mm. The filamentation phenomenon is also observed in the 3D simulation.[76]

The surface tension-driven 3D model in *FLOW-3D* is highly computationally demanding. As a remedy, further investigation on the pressure gradient, shear rate, and shear stress during the roll-coating is conducted in two-dimension. The cross-sectional view of the fluid at the roller's interface is shown in Figure S5a (Supporting Information). The pressure gradient (dp/dx) and fluid velocity (V_x) are observed along the x-axis (a-b direction).
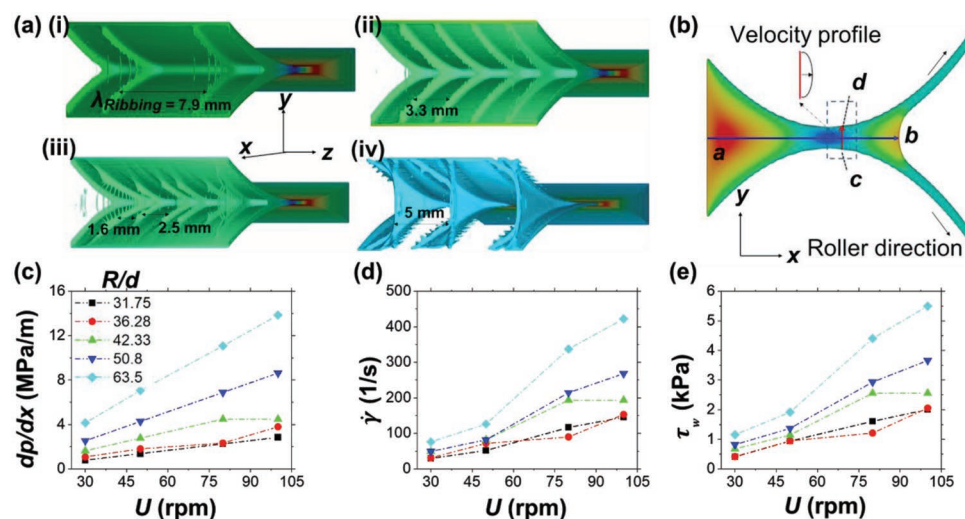

Figure 2. a) Ribbing instability observed in CFD simulation. The displayed images are for roller speeds of 40 rad s^{-1} and R/d (i) 63.5 (ii) 84.67 (iii) 101.6, and (iv) 127. b) Cross-section of the fluid profile showing the velocity and pressure gradient. c–e) Pressure gradient in the flow direction dp/dx, shear rate $\dot{\gamma}$, and wall shear stress τ_w in various roller speeds (U of 30, 50, 80, and 100 rpm) and roller distances (at R/d of 31.75, 36.29, 42.33, 50.8, and 63.5).
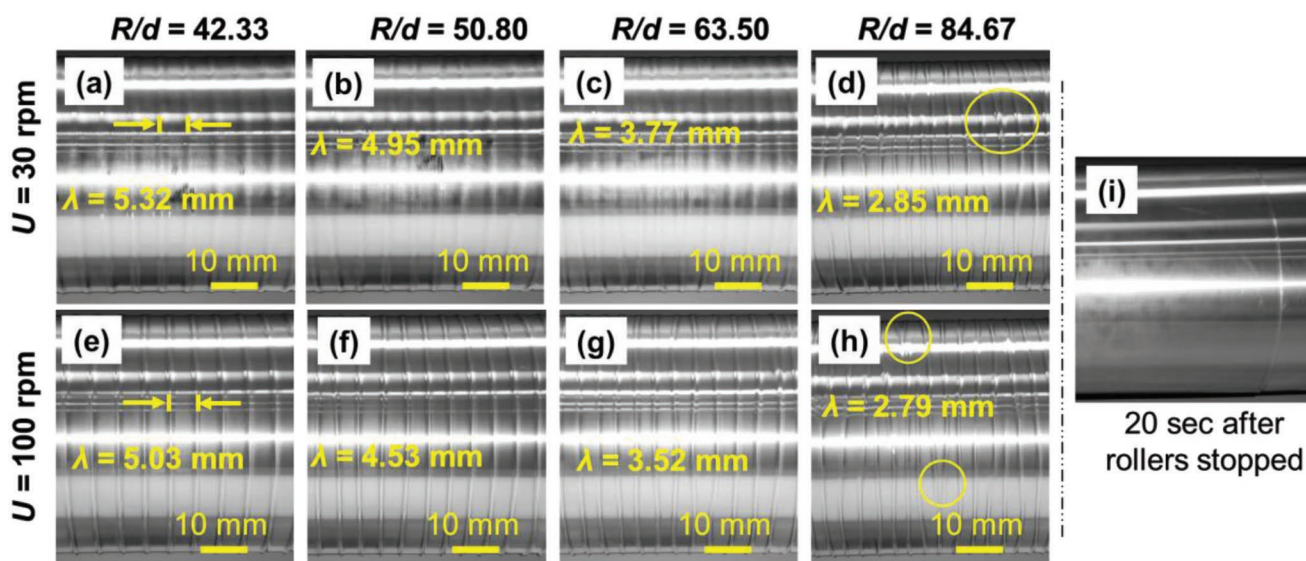
Figure 3. a–h) Ribbing instability of PDMS under various process conditions; i) PDMS flattens after a few seconds.

As the rollers begin to rotate, a pressure differential is generated, as observed in Figure S5b (Supporting Information), with high pressure on the upstream, which drives the fluid flow. The pressure differential increases with an increase in R/d. The higher-pressure differential also causes a higher V_x in the a-b direction. The V_x is also plotted against y/d in the c-d direction (Figure S5c, Supporting Information), where y is the coordinates in the y-direction and d is the roller distance. The maximum velocity of the PDMS is observed at the center of the fluid flow, $x/d = 0.5$ (Figure S5c, Supporting Information). The shear rate was next calculated as the velocity gradient (dV_x/dx) and presented in Figure S5d (Supporting Information). The maximum shear occurs at the roller's wall and the higher R/d results in the higher shear rate. Next, a parametric study is conducted for roller speed (U) of 30, 50, 80, and 100 rpm with R/d of 31.75, 36.28, 42.33, 50.8, and 63.5. The resulting dp/dx, $\dot{\gamma}$, and τ_w are plotted in Figure 4f–h. Each of these parameters increases with an increase in roller speed and R/d. The effect of R/d was more dramatic at higher roller speed. For example, the dp/dx increases only from 0.79 to 4.14 MPa m^{-1} at 30 rpm but increases from 2.84 to 13.86 MPa m^{-1} at 100 rpm. Similarly, at R/d of 31.75, the dp/dx increases from 0.79 to 2.84 MPa m^{-1} as the roller speed increases from 30 to 100 rpm, respectively, whereas the same increase in speed causes dp/dx to escalate from 4.13 to 13.86, respectively. In summary, the CFD analysis established a method to determine some key parameters that were not able to examine in prior studies due to the limitation of the experimental tools. The dp/dx, $\dot{\gamma}$, and τ_w observed in the CFD simulation results is utilized to analyze the experimental results in the following sections.

2.2.2. Ribbing Instabilities in Roll-Coating of PDMS

A parametric study was conducted for PDMS as the coating liquid to understand the ribbing behavior related to the process parameters. Upon rotation of the rollers, a distinct ribbing phenomenon is observed, identical to what was observed in the CFD simulation in Figure 2a. The ribbing wavelength ($\lambda_{Ribbing}$) is defined by the distance between each riblet's peak. Some of the ribbing images are shown in **Figure 3**a–h. The ribbing wavelength ($\lambda_{Ribbing}$) is investigated concerning the rollers speed (U) and the dimensionless geometric parameter R/d. For any given R/d, an increase in roller speed results in a decrease of $\lambda_{Ribbing}$ (**Figure 4**a). A more dramatic reduction in wavelength is observed with the rise of R/d for any specific speed. For example, at R/d 31.75, the wavelength decreases from 7.03 to 6.47 mm with a 30–100 rpm roller speed. At 30 rpm speed, the wavelength reduces from 7.03 to 3.52 mm as the R/d increases from 31.75 to 63.5, respectively. At a higher R/d (>63.5), the linear ribbing periodicity started to be nonuniform (Figure 3h), similar to what was observed in the CFD simulation (Figure 2a).

The ribbing pattern of the PDMS is only observed when the rollers are rotating. As soon as the rollers stop, the ribbing patterns flatten in a few seconds due to the surface tension (Figure 3i). As observed in Section 2.1, the PDMS behaves like a fluid with nearly constant viscosity (about 5.2 Pa s) from a shear rate of 0.1 to 100 s^{-1}. This fluid-like behavior allows the surface tension force to flatten the ribbing patterns quickly.

The calculated dp/dx, $\dot{\gamma}$, and τ_w from the CFD simulations are plotted against the experimental wavelengths (Figure 4b–d). As also supported by the earlier studies,[36] the dp/dx was closely related to the ribbing wavelengths. A higher dp/dx associated with more instabilities resulted in shorter wavelengths. In addition higher $\dot{\gamma}$, and τ_w also resulted in shorter ribbing wavelengths. A statistical analysis of the $\lambda_{Ribbing}$ individually with respect to $\log_{10}(dp/dx)$, $\log_{10}(\dot{\gamma})$, and $\log_{10}(\tau_w)$ shows a correlation factor of −0.836, −0.81, and −0.823, respectively, proving a strong relationship between these parameters. In addition, a linear fitting between these parameters also shows R-square values of 0.68, 0.64, and 0.66 consecutively for the equations shown in Figure 4b–d. A lack of fitting analysis for the linear fitting results in a p-value of 0.056, 0.243, and 0.25. This demonstrates that the fittings are significant with 95% confidence (p-value > 0.05).

**ADVANCED
SCIENCE NEWS**

www.advancedsciencenews.com

**ADVANCED
MATERIALS
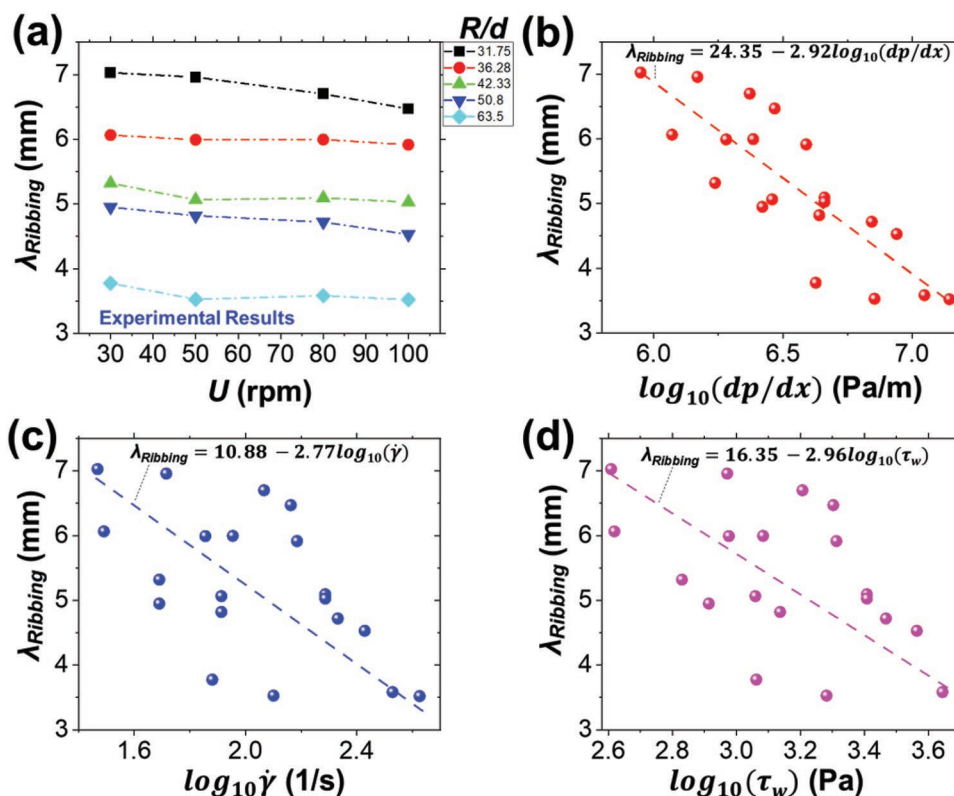INTERFACES**

www.advmatinterfaces.de

Figure 4. a) Experimental data of PDMS ribbing wavelengths versus various process conditions. b–d) The experimental wavelengths of PDMS are plotted against $\log_{10}(dp/dx)$, $\log_{10}(\dot{\gamma})$, and $\log_{10}(\tau_w)$ calculated from the CFD analysis.

In summary, there were two crucial findings from the roll-coating of the PDMS. The wavelength decreases with an increase in roller speed or R/d, whereas the reduction is more evident with the rise of R/d. The dp/dx, $\dot{\gamma}$, and τ_w drive the wavelength formation. The PDMS cannot retain the ribbing patterns when the rollers stop as the materials behave as a fluid. This draws interest in synthesizing coating materials that will behave as a solid when at rest, preventing surface tension-driven flattening, but acts as fluid during the roll-coating allowing the ribbing formation to occur.

2.2.3. Ribbing Instabilities in Roll-Coating of CNT-PDMS Composite

The CNTs were next introduced into the PDMS to tailor the viscoelastic properties of the coating materials. A yielding material is necessary to avoid surface flattening when the rollers stop, which will selectively behave like a fluid in elevated shear stress but behave as a solid when the stress is unloaded. The entanglement of the cylindrical-shaped CNTs allowed such behavior. Composite paste with various concentrations of the CNTs was synthesized and utilized in the roll-coating process. At first, 0.5 and 1 wt% CNT were added to the PDMS matrix, and the roll-coating was observed in a high-speed camera.

Similar to the PDMS, ribbing formation is observed for 0.5 wt% CNT-PDMS composite (Figure S6a, Supporting Information). However, another phenomenon known as

filamentation was also observed during the roll-coating.[76] A small hole appears, generating a filament at the roller's interface. As the roller rotates, the hole becomes more prominent as the filament stretches, eventually breaking and developing a peak on top of the ribs (Figure S6d, Supporting Information). The produced surface is thus a hybrid of ribbing formation and peaks from filamentation rupture. The elastic relaxation of the composite paste has a crucial effect in generating such micropeaks, with lower elastic materials expected to have shorter peaks.[76] Future studies will investigate the extensional viscoelasticity of the composite paste and how it influences the instabilities in roll-coating.

The high-speed images of roll-coating with 1 wt% of CNT-PDMS are shown in Figure S7 (Supporting Information). Roller speeds of 20, 60, and 100 rpm and R/d of 50.8, 63.5, and 84.67 are presented. The observed hybrid pattern is similar to 0.5 wt% CNT-PDMS results. At 20 rpm speed, the wavelength reduces from 1.03 to 0.49 mm with an R/d increment from 50.8 to 84.67. Notice that the ribbing wavelengths in PDMS ranged from 2.8 to 5.32 mm, whereas the wavelength significantly reduced with the addition of CNTs. This is primarily due to the higher viscosity of the coating paste, causing more dramatic dp/dx resulting in a shorter wavelength. In addition, the linearity of the wavelength formation is also compromised at higher speed and R/d.

The roll coating of 0.5 and 1 wt% CNT-PDMS provided essential understanding. i) The wavelength reduced significantly compared to the PDMS as the viscosity and elasticity
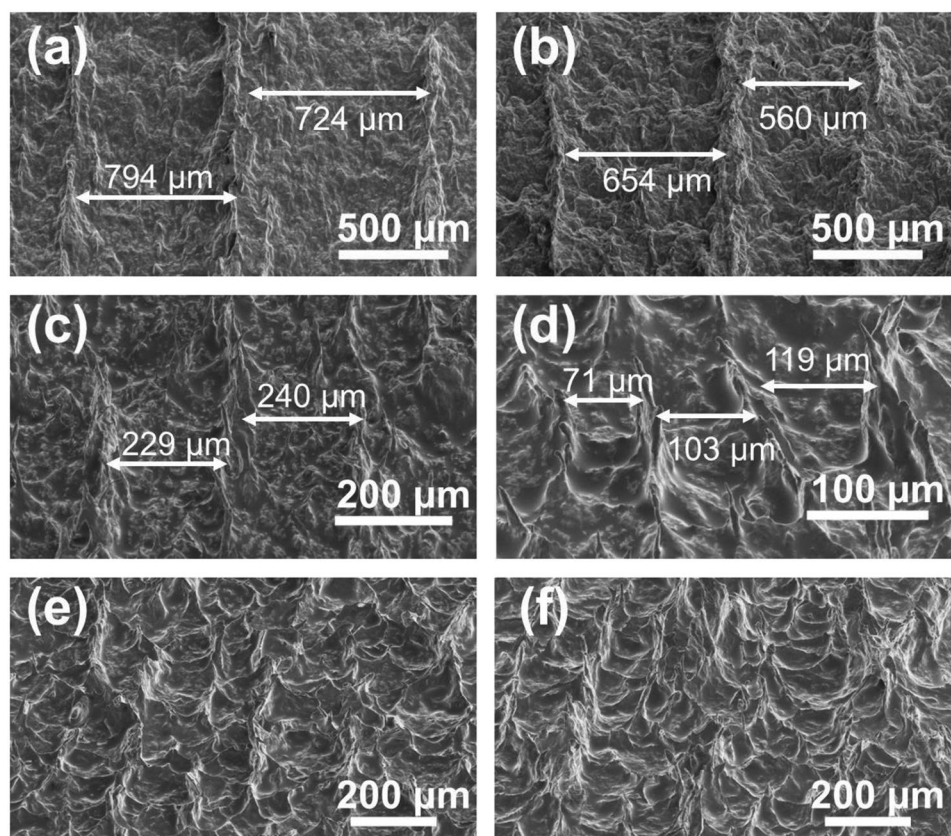
Figure 5. SEM image of fabricated samples at 20 rpm speed, and a) R/d = 56.44; b) R/d = 63.50; c) R/d = 72.57; d) R/d = 84.67; e) R/d = 101.60; f) R/d = 127.

increased. ii) An additional mode for pattern formation known as filamentation was also observed, which affects the final patterns. iii) At a lower velocity, it was observed that the patterns were more likely to align linearly. iv) In addition, the wavelength control was more precise by controlling the R/d, which is also observed in the roll coating of the PDMS. These findings guided subsequent experimentation with higher wt% CNTs for potentially reducing ribbing wavelength in the micrometer range.

Coating pastes were prepared by adding various wt% of CNTs to the PDMS. 3–3.5 wt% CNT-PDMS provided the most linearly periodic samples upon extensive experimentation. As the wt% of CNTs increases, the higher viscosity and elasticity cause the generated pattern to be more random. For example, no forms of linearity were observed in roll-coating samples with >5 wt% CNTs. The 3 wt% CNT-PDMS sample showed ribbing instabilities and produced a microtrench profile at R/d = 63.5 at 50 rpm roller speed (Figure S8a, Supporting Information). However, an attempt to further reduce the ribbing wavelength by increasing the R/d resulted in a linear to vein-leaf shape transition at R/d = 84.67. A further increase in R/d to 101.6 results in vein-leaf shape samples with a high aspect ratio with a large ribbing wavelength at a millimeter scale. Thus, a more viscous material, 3.5 wt% CNT-PDMS, was utilized to prepare the final samples and further reduce the microstructured surface's wavelength. The roller's speed was fixed at 20 rpm, while the R/d varied from 56.44 to 127.

2.3. Morphology Characterization and Performance Analysis of Periodic Microstructure

2.3.1. Surface Morphology Analysis

The 3.5 wt% CNT-PDMS samples showed a hybrid microstructure created by ribbing and filamentation similar to 0.5 and 1 wt% CNT-PDMS. While the ribbing waves were observed transverse to the roll-coating direction, filamentation resulted in many micropeaks in the longitudinal direction. The SEM images of the samples are shown in **Figure 5**. The R/d = 56.44, 63.50, 72.57, and 84.67 showed mostly linear ribbing formation, whereas the R/d = 101.60 transitioned to a more random microstructure. Despite less consistent microtrenches in comparison to 3 wt% CNT-PDMS samples, it was possible to achieve shorter $\lambda_{Ribbing}$. The randomness increased to taller features at R/d of 127. The ribbing wavelengths were reduced from 700 to 90 μm for the linear-microstructure sample (Figure 5a–d). The (R/d = 101, 127) sample showed highly dense micropeaks and a high aspect ratio. The entangled CNTs with their yield stress allowed the PDMS to retain the complex microstructure after roll-coating by resisting the surface tension-driven flattening.

Since the SEM shows only a small area of the samples, a laser confocal microscope was utilized to quantify the wavelengths and surface roughness. **Figure 6**a shows an example of samples' 3D topography. The ribbing wavelength ($\lambda_{Ribbing}$), as described earlier, is defined as the distance between each
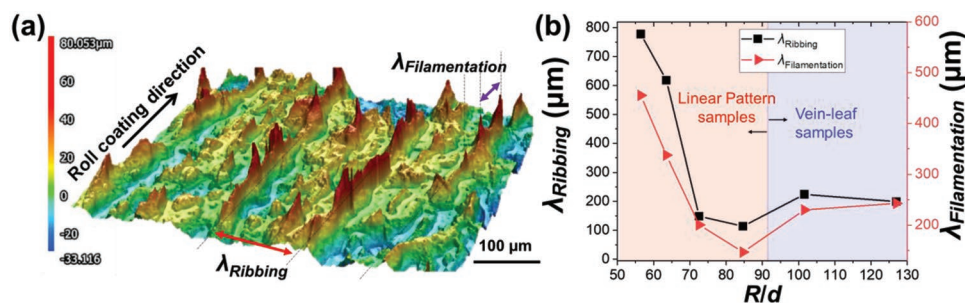
ADVANCED
SCIENCE NEWS
www.advancedsciencenews.com

ADVANCED
MATERIALS
INTERFACES
www.advmatinterfaces.de

Figure 6. a) Laser confocal microscope image of the fabricated sample showing both ribbing and filamentation phenomenon; b) $\lambda_{Ribbing}$ and $\lambda_{Filamentation}$ versus R/d.

transverse riblet. The filamentation wavelength ($\lambda_{Filamentation}$) is the peak-to-peak distance in the longitudinal direction, as shown in Figure 6a. The samples included random microstructures along with linearly periodic patterns. To quantify the wavelengths, multiple (>20) transverse and longitudinal lines (were drawn on the 3D surface with the Multifile-analyzer software (Keyence). Each of these lines showed the peaks and valleys of the surface topography. The wavelengths for these individual lines are evaluated by the software, and the mean and SD values are presented in Table S2 (Supporting Information) and plotted in Figure 6b. The wavelengths reduce for both ribbing and filamentation phenomenon with an increase in R/d, associated with more instabilities. The average $\lambda_{Ribbing}$ was 777, 618, 148, and 114 µm for the R/d = 56.44, 63.50, 72.57, and 84.67 samples. However, when the linear microstructure transitions to a random microstructure at R/d = 101.60, the wavelength increases to 224 µm. The average $\lambda_{Filamentation}$ also follows the same pattern as the observed wavelengths were 455, 337, 200, 146, 230, and 242.98 µm for the R/d = 56.44, 63.50, 72.57, 84.67, 101.60, and 127. The Wenzel roughness factor (r) was also evaluated, which is discussed in the following section in conjunction with the water contact angle measurement result.

The water contact angles (WCA) of the microstructured samples were measured to demonstrate the hydrophobicity of the surface (**Figure 7**). The measurement was done in five different locations for each of the samples (Table S2, Supporting Information). The average WCA of the linear microstructured samples were 128.17°, 133.64°, 136.98°, and 137.27° for R/d = 56.44, 63.5, 72.57, and 84.67, respectively. In comparison, a compression-molded flat CNT-PDMS sample showed a WCA of 115.4°. Thus the increased WCA to R/d is related to the roughness of the fabricated sample. However, the trend stalls right before transitioning from a linearly periodic microstructure to a high aspect-ratio random microstructure. The WCA dramatically increases into the superhydrophobic range to 150.63° and 158.13° for R/d = 101.6 and 127. This is primarily due to the increase in the surface area of the samples due to enhanced hierarchical structure geometry, which is also reflected in the high Wenzel roughness factor of ≈3.5. The WCA and the Wenzel roughness factors matched well (Figure 7b). The water droplets images for the highest observed WCA are shown in Figure 7c.

The roll-coated samples were broadly classified into two categories based on the microstructures. The generated patterns were mostly linearly periodic samples for the 3.5 wt% CNT-PDMS samples with 20 rpm speed and $R/d \leq 84.67$ (Figure 5).
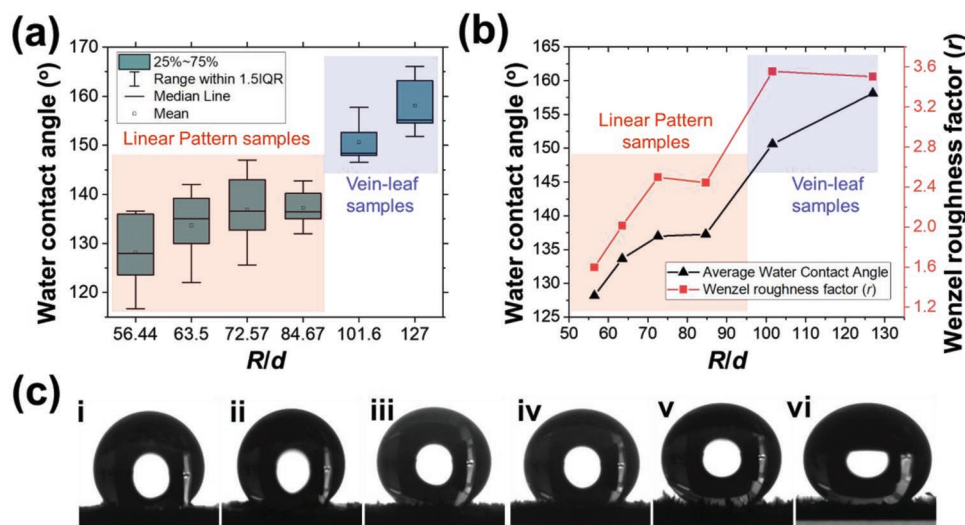

Figure 7. a) Water contact angle measurements boxplot in five different locations of each sample. b) Average water contact angle and Wenzel roughness factor vs. R/d. c) Droplet images are the highest contact angle obtained for R/d ratio of (i) 56.44, (ii) 63.5, (iii) 72.57, (iv) 84.67, (v) 101.6, and (vi) 127.

Whereas samples with R/d 101.6 and 127 showed more vein-leaf shape structure with high aspect ratios. The results indicate a significant alteration in the ribbing formation after the critical R/d value of 84.67. However, since the roll-coating experiment itself could not provide further information on the state of the coating paste, such as the fluid velocity, pressure gradient, shear rate, and wall shear stress, further CFD analysis was conducted to evaluate these parameters and potentially correlate with the experimental results observed by the SEM and laser confocal.

The pressure gradient in the direction of fluid flow, dp/dx for 3.5 wt% CNT-PDMS, was observed to be an order of magnitude higher than PDMS. The dp/dx ranged from 667 to 3138 MPa m^{-1} for R/d of 56.4 to 127 (**Figure 8**a). The enormous increase in pressure gradient is sourced from the elastic nature of the viscoelastic fluid, which restricts the flow and increases the stress significantly.[49] The high dp/dx results in much more aggressive ribbing instability even at a slower roller speed than PDMS. The associated shear rate during the roll-coating experiments was also evaluated based on the CFD analysis. The roll coating of 3.5 wt% CNT-PDMS at 20 rpm speed results in 54.02, 80.81, 93.04, 116.37, 119.87, and 154 s^{-1} shear rate for R/d of 56.44, 63.5, 72.57, 84.67, 101.6, and 127. Notice that the wall shear stress steadily increases from 0.3 to 0.41 MPa for R/d of 56.44 to 84.67. However, at R/d 101.6, when the shear rate is 119.87 s^{-1} the wall shear stress increases sharply to 0.45 MPa (Figure 8b). As observed in prior studies, the abrupt change in wall shear stress results in further tip-splitting, which results in the vein-leaf shape structure. Grillet et al. observed similar tip-splitting behavior specifically for elastic materials and noticed that an increased elasticity dramatically changes the shape structure to be more random.[43] The CFD analysis of the roll coating of 3.5 wt% CNT-PDMS helped to uncover the critical roll coating process parameter along with the associated dp/dx, $\dot{\gamma}$, and τ_w that contribute for the transitions between the linear to vein-leaf shape formation.

2.3.2. Hydrodynamic Drag Reduction

The hydrodynamic drag reduction of the linear microstructured sample was measured by attaching the sample to the underside of a miniature boat and pulling it parallel to the water surface using a wire-and-pulley system (**Figure 9**). A weight was used to create a steady tension in the wire that pulls the boat with a constant force. Four different loads (1.7, 0.8, 0.6, and 0.5 g) were used for the boat to reach four different steady speeds. The time it took for the boats to travel a set distance (180 cm) was measured, and the acceleration time was short enough to be ignored. The velocity, acceleration, Reynolds number (Re), and Froude number (Fr) of the boat and the velocity increase of the boats with the linear microstructured sample relative to the ones without were calculated from the measured times. For Reynolds numbers 55 397, 33 163, 20 677, and 15 348, the velocity increases (or drag reductions) were 8.27%, 8.68%, 7.31%, and 4.34%, respectively. This decrease of drag reduction with increasing Reynolds number, which deviates from what is known for laminar flows,[77] can be explained by the large Froude number even at low Reynolds numbers due to the small boat size. Note that the boat's drag in the current experiment comprises skin friction and wave-making, and the given sample can reduce only the skin-friction drag with no effect on the wave-making drag. When $Fr < 0.25$, the skin friction drag is dominant; however, the wave-making resistance dominates when $Fr > 0.25$.[78] When the Froude number increased (0.13, 0.18, 0.29, and 0.48, correspondingly) so that the portion of skin friction in the total drag decreased, the reduction of skin friction had a diminishing effect on the total drag. The sample with the densest linear patterns ($R/d = 84.67$, $\lambda_{Ribbing} = 114$ µm) was the most significant drag-reduction reported in this section. The samples with broader wavelengths did not have a conclusive result as they lack the ability to retain the plastorn.

2.3.3. Electrical Conductivity Measurements

Adding a conductive filler in a nonconductive polymer matrix was found to incur electrical conductivity based on prior studies.[79–81] Such reinforcement by mechanical-mixing procedure was also observed to improve the electrical and mechanical properties simultaneously.[88–90] Since CNTs are highly conductive, there is a potentiality of achieving multifunctionality of the SHPo samples if electrical conductivity is also observed. The electrical sheet resistance of the samples
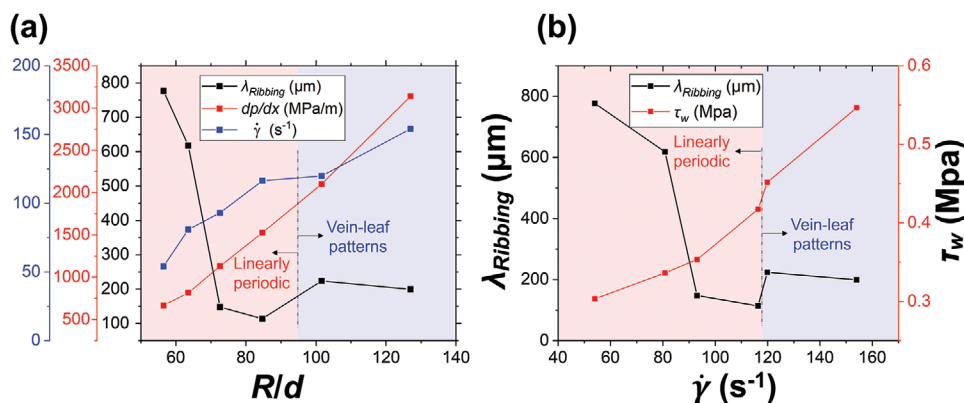

Figure 8. CFD simulation results for roll-coating of 3.5 wt% CNT-PDMS under various process conditions (a) $\lambda_{Ribbing}$, dp/dx, and $\dot{\gamma}$ vs. R/d. (b) $\lambda_{Ribbing}$ and wall shear stress vs. shear rate.
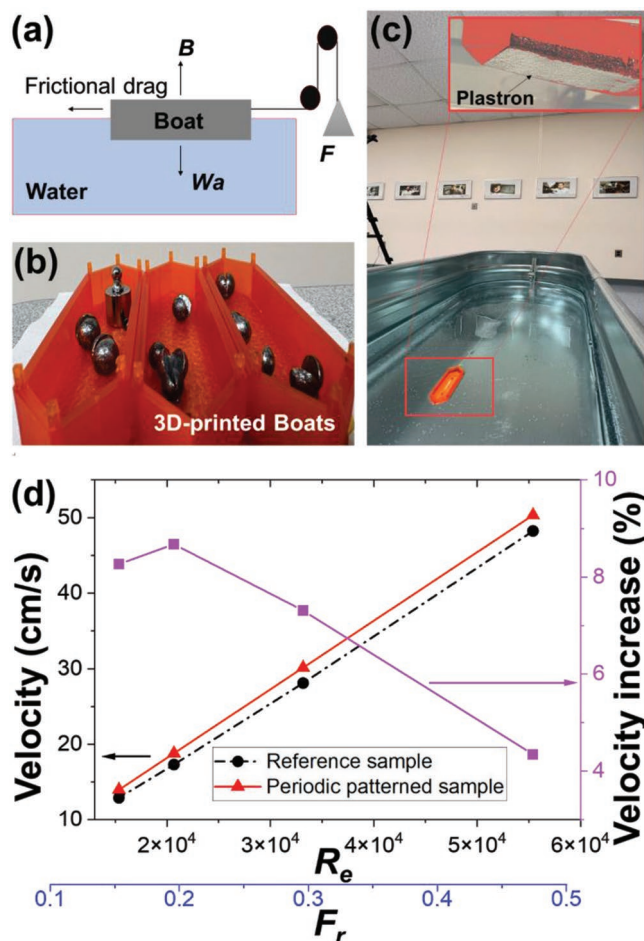
Figure 9. a) The free-body diagram of drag-reduction experimental setup. b) Miniature model boats with standard loads. c) Experimental setup. d) Velocity profile of model boat with and without the linear microstructured sample.

Figure 10. Sheet resistance R_s of the CNT-PDMS composite samples.

was measured by a custom-made four-point setup following the Van der Paw method with varying CNT wt% and is represented in **Figure 10**. It was found that CNT wt% of 0.5, 1.0, 1.5, 2.0, and 2.5 had sheet resistance values of 747.84, 190.36, 90.64, 36.26, and 22.66 $\Omega \ \square^{-1}$, respectively. The decrease in sheet resistance because of increased CNTs creates a percolated network. As observed in Figure S3 (Supporting Information), the CNTs form a percolated network in PDMS which is attributed to the enhanced electrical conductivity. As more CNTs are added, the percolation increases until a certain percolation threshold.

In a percolated network, electrons move across the network under an applied electrical field, which increases electrical conductivity.[82] This increase in electrical conductivity, therefore, decreases the measured sheet resistance. Thus, as more CNTs are added, the percolated network grows and enables a decrease in the sheet resistance by increasing electrical conductivity. The PDMS-Sylgard 184 sample resistance was undetermined in the experiment, possibly due to very high resistivity.

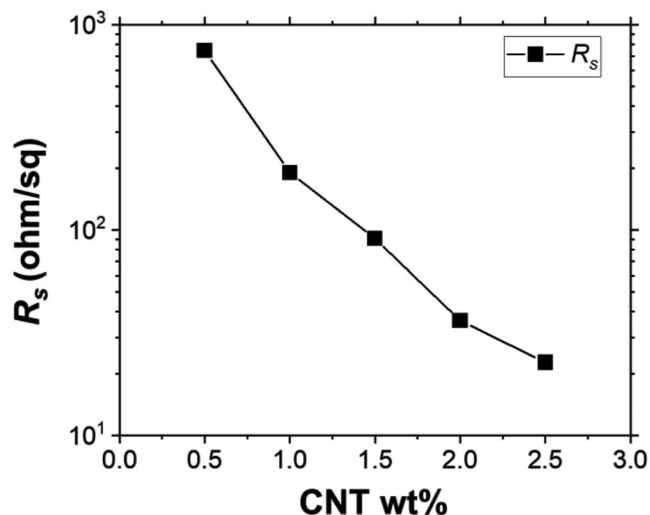This is also important to mention that Lee et al.[83] and Xu et al.,[84] worked on manufacturing SHPo surfaces capable of plastron regeneration primarily by attaching additional conductive electrodes integrated into the surface, which allowed plastron regeneration by electrolysis when the water began to penetrate the microtrench cavities. However, the microtrench structure fabricated in the present study would also be able to regenerate plastrons without additional electrode molding since the CNT-PDMS material is reasonably conductive. Further studies will be conducted in the future, focusing on the plastron regeneration capabilities of the manufactured SHPo surface in the presented study.

2.3.4. Scratch Testing

The robustness of the 3.5 wt% CNT-PDMS microstructured sample was tested to identify the critical load of cohesive and adhesive failure. The critical load is the smallest load that causes microstructural damage for possible cracking or plastic deformation.[85,86] Although this test is not a comprehensive materials property test as the test parameters also have an effect, the critical load observed in such a scratch test is also a function of the mechanical strength of the materials. The first mode of failure, or the cohesive failure (L_{C1}) in the CNT-PDMS sample, was observed for 7 N force as there seemed to be a sudden increase in the frictional force (**Figure 11**). The secondary failure was observed at 16 N, the adhesive failure between the test sample and the substrate. The frictional coefficient for the 3.5 wt% CNT-PDMS composite was stable at ≈0.2. Compared to the CNT-PDMS sample, the PDMS sample's cohesive failure occurred at a lower force of 3.6 N. The adhesive failure (L_{C2}) was similar to the CNT-PDMS sample of 15.8 N force. The frictional coefficient of the PDMS sample seems to be much higher (≈0.35–0.45) than the CNT-PDMS sample. The microstructured surface assisted in this reduction in tribological friction, as observed in other studies.[17,87] The CNT addition helped the composite layer achieve superior mechanical properties compared to pure PDMS. As observed in Figure S3 (Supporting Information), the entangled CNTs physically interlock the PDMS from slippage and improve the mechanical
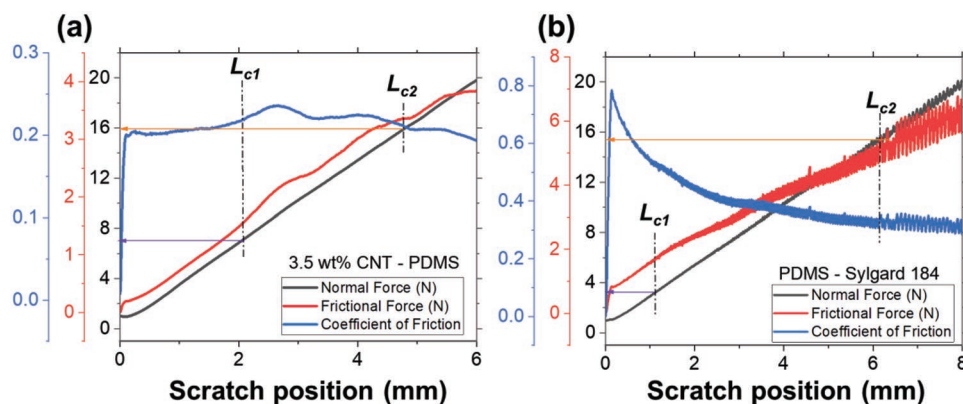
Figure 11. Scratch test of a) 3.5 wt% CNT-PDMS sample and b) PDMS-Sylgard 184 sample.

properties. Future studies will include the wear properties of the CNT-PDMS microstructures layer and underwater testing for a prolonged time to observe possible material degradation.

3. Conclusion

A comprehensive investigation was conducted to study the ribbing formation during a roll-coating process both computationally and experimentally. First, ribbing instabilities for the pure PDMS were investigated. It was found that the pressure gradient occurring due to roller speed, R/d, and the material's viscoelastic properties is the key driving force of the ribbing instabilities. The wavelengths for the PDMS were observed in the 7.03–3.52 mm range for roller speeds from 30 to 100 rpm and R/d of 31.75 to 63.50. The ribbing formation of PDMS was also observed to flatten when the roller stops due to lower surface energy compared to the viscosity and also not having yield stress. Increasing the CNT content on the PDMS allows the polymer to retain its solid shape even after stopped roll-coating as yield stress of 0.0025, 0.01247, and 0.08737 MPa was observed for 1, 3.5, and 10 wt% of CNT-PDMS. The observed microstructure of the surfaces by the roll-coating was characterized as a hybrid pattern due to ribbing instability and filamentation due to elastic relaxation of the coating paste.

The manufactured samples showed a controllable 114–777 µm size. However, as the roller distance decreases further to increase the R/d to 101.60, the linear ribbing transitions into the random microstructure with a high Wenzel roughness factor (r) of 3.56. The water contact angle of the samples ranged from 128.17° to 158.63°. The CNTs addition also made the samples conductive, opening opportunities for multifunctional applications. The mechanical durability of the fabricated microstructures is also investigated by scratch testing. Finally, the fabricated pieces are also being used to demonstrate drag-reduction capabilities in miniature model ships, self-cleaning surfaces, and anti-biofouling applications.

This study demonstrated a simple, scalable fabrication process to achieve periodic microstructures. The research helped to carefully identify and narrow down the suitable material composition and process parameters to control the microtrenches' periodicity. However, the periodicity and uniformity in the produced samples are not close to the photolithography-based manufactured samples. The presented new technique has enormous potential moving forward for scalable manufacturing. The complete sample preparation requires only half an hour, beginning with the coating paste preparation, roll-coating, and heat-curing. The maximum size achievable with the presented two-roll-coater is 300 mm × 150 mm, only constrained by the diameter and length of the rollers. Taking advantage of the ribbing instabilities, a large periodic microstructured surface can be obtained quickly by employing a more robust roll-coater with continuous substrate-feeding capabilities. Future work will be focused on fine-tuning the process parameters, including a new materials system to improve the control of the surface morphology to move closer to the photolithography-based techniques.

4. Experimental Section

Coating Materials Preparation: A nanocomposite paste was synthesized using a polydimethylsiloxane elastomer kit (PDMS Sylgard 184, Dow chemicals) and a multiwalled CNT (6–9 nm diameter and 100–200 µm length). The PDMS and CNTs were initially mixed utilizing a universal planetary mixer for 10 min (**Figure 12**). Next, the hardener was introduced to the PDMS with a 10:1 ratio. This mixture was then mixed further in a high-shear three-roll milling machine. The roller distances were gradually reduced, and the materials were passed through multiple times to ensure adequate dispersion and homogenization of the CNTs. The wt% of the CNT was varied to achieve composite pastes with tailored rheological properties.

Forward Roll Coating: A two-roll coating machine was utilized to fabricate the samples and analyze the ribbing behavior (**Figure 13**a). Each with a radius (R) of 25.4 mm, the rollers run with independent motors that can control the angular speed from 0 to 120 rpm. To transfer the composite film after roll-coating, a removable polyimide sleeve was inserted on roller #1. The coating materials were inserted between two rollers and were introduced to different process conditions by controlling the roller velocities U and the roller distance of d (Figure 13b). Finally, the microstructure composite film was oven-cured at 125 °C for 25 min. An example of a roll-coated sample with linearly periodic microstructure is shown in Figure 13d,e and a vein-leaf patterned microstructure in Figure 13f,g.

CFD Simulation: Simulations of the roll coating process were performed using the commercial computational fluid dynamics software *FLOW-3D* based on the volume of fluid (VOF) method. The schematic of the simulation configuration with boundary conditions is shown in **Figure 14**. The fluid flow inlet is considered a pressure boundary condition with fluid fraction of 1, whereas an outflow boundary condition is used at the outlet. All other boundaries are assumed symmetric.
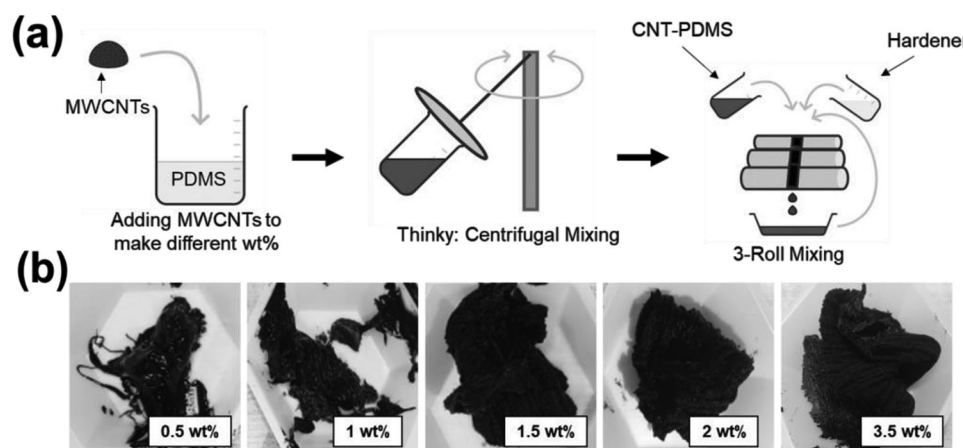
ADVANCED
SCIENCE NEWS
www.advancedsciencenews.com

ADVANCED
MATERIALS
INTERFACES
www.advmatinterfaces.de

Figure 12. a) Coating paste formulation. b) Processed CNT-PDMS with varying wt%.

The gravity and noninertial references, surface tension, viscosity, and turbulence physics modules were utilized in the simulation. The PDMS (Sylgard-184) and 3.5 wt% CNT-PDMS were modeled based on the surface energy and viscosity measured experimentally in this research. The unsplit-Lagrangian model was used for the volume of fluid advection scheme. The fluid flow was solved using Navier–Stokes momentum and continuity equations. A minimum time step of 10^{-16} s and a maximum time step of 10^{-7} s were considered with a 5% volume-fraction cleanup to minimize computation time. *FLOW-3D* POST was utilized to the analyzing the simulation results.

Rheology Measurement: Dynamic oscillatory rheological experiments were conducted on a Discovery Hybrid 3 rheometer (TA Instruments) and performed in triplicate. Creep experiments were also conducted to confirm yield stress values. All experiments were performed using an 8 mm cross-hatched parallel plate geometry kept at 25 °C by using a Peltier plate. Since the samples were high modulus pastes, the samples were loaded in excess via spatula or by a gloved hand. The rheometer head was brought down to an 1100 µm trim gap, then brought to 1000 µm after trimming. Since the sample would eject in a shear deformation, no preshearing was performed, and the test was performed right away, as viscometric parameters did not change with time after loading.

The samples' linear viscoelastic (LVE) region and yield stress were determined using a strain sweep. Frequency sweeps were performed from 0.1 to 100 Hz at an oscillatory strain of 0.1% in the LVE region. The yield stress was determined by evaluating the maximum of elastic stress, which is a product of elastic modulus and strain, with respect to strain. The stress associated with strain is the yield stress, which is in
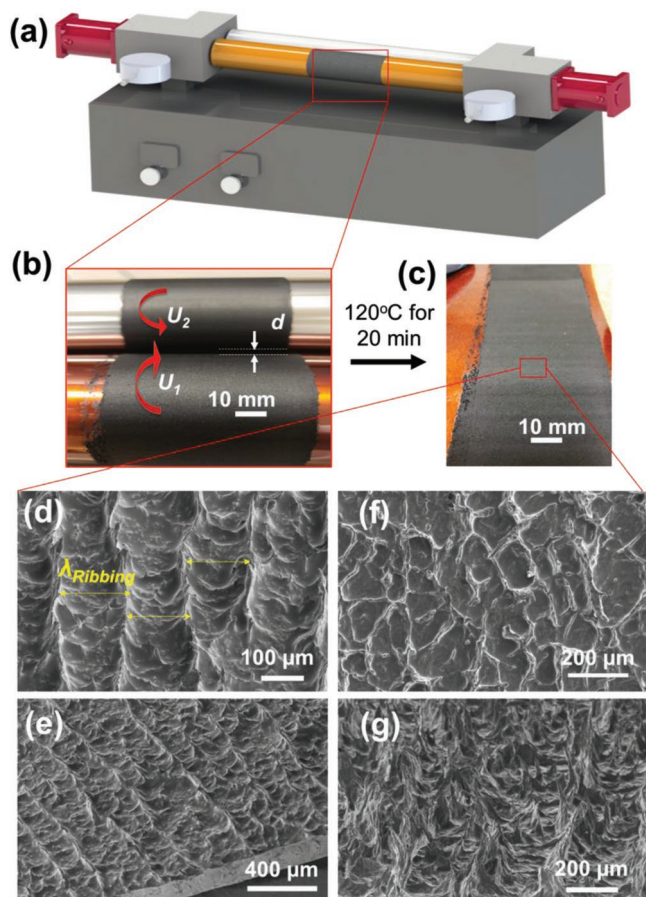

Figure 13. a) Two roll coating machines; b) forward roll coating of composite paste; c) fabricated sample after heat-cure. d,e) SEM image showing the microtrench formation and the peak formations due to fil-amentation on a linearly periodic sample. f,g) SEM images show high aspect ratio vein-leaf shape samples, as the *R/d* crosses a critical value.
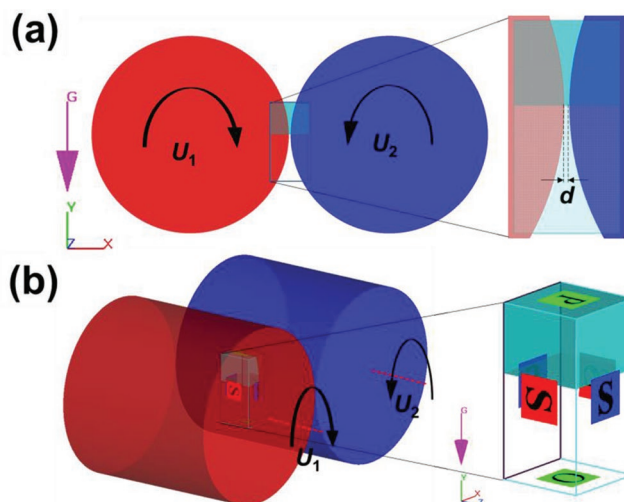

Figure 14. Schematic of the CFD simulation configuration of the two-roll coater in a) 2D and b) 3D. The inset image shows the fluid-flow mesh boundary conditions.

Table 1. Polar and dispersive surface energy components of the test liquids.[95]

Test liquid	γ_l [mJ m^{-2}]	γ_l^p [mJ m^{-2}]	γ_l^d [mJ m^{-2}]
Water	72.8	51.0	21.8
Diiodomethane (DIM)	50.8	0.0	50.8
Ethylene glycol (EG)	48.0	19.0	29.0

accordance with Walls et al.[91] A creep test was performed on a 10 wt% sample to confirm the yield stress measurements.

Surface Energy Measurement: Several surface energy theories were developed based on the contact angle and θ measurements. Fowke's model[92] and the Owens–Wendt model[93,94] were utilized in this study. Fowke's model combines the Young and Young–Dupree equations and separates liquid and solid surface energy as polar and nonpolar components as Equation (1)

$$\frac{\gamma_l(\cos\theta + 1)}{2} = (\gamma_l^d)^{1/2}(\gamma_s^d)^{1/2} + (\gamma_l^p)^{1/2}(\gamma_s^p)^{1/2} \tag{1}$$

Here, γ_l^d and γ_l^p are liquid nonpolar (dispersive) and polar components, respectively. Whereas γ_s^d and γ_s^p are the solid nonpolar and polar components. The Owens–Wendt model, also known as the extended Fowke's model, incorporates the Good's equation, thus resulting in Equation (2)

$$\frac{\gamma_l(\cos\theta + 1)}{2(\gamma_l^d)^{1/2}} = (\gamma_s^d)^{1/2} + \frac{(\gamma_l^p)^{1/2}(\gamma_s^p)^{1/2}}{(\gamma_l^d)^{1/2}} \tag{2}$$

Three reference liquids with known surface energy values, as mentioned in **Table 1** (e.g., water, diiodomethane (99%), and ethylene glycol (99%)), were utilized to measure the contact angle on a flat-surfaced test sample. The results were fitted into Equations (1) and (2) to evaluate the surface energy of the test material by Fowke's model and Owens–Wendt's model. The test samples were prepared by a compression molding method, as shown in Figure 12a. The CNT-PDMS-hardener compositions were mixed well in the Thinky mixer and the three-roll-mill. The resulted composition was placed between two polyamide sheets and compression-molded under 1 ton pressure with a 0.5 mm spacer (**Figure 16**a). The polyamide sheet with the CNT-PDMS composite was next heat-cured at 120 °C for 20 min. The polyamide sheet was quickly removed as the polymer crosslinked, resulting in a flat circular-shaped composite sample with uniform thickness. The surface roughness of these test samples was measured using a laser confocal microscope that accounts for surface roughness in the surface energy measurement calculation.

Surface Morphology Characterization: The surface roughness and waviness of the samples were characterized by a noncontacting laser scanning confocal microscope (Keyence VK-X1100, 0.5 nm height resolution, and 1 nm width resolution). The Wenzel roughness factor (r) and arithmetic mean wavelength (λ) were evaluated from the laser confocal data. The surface morphology was also investigated with a high-resolution scanning electron microscope (FEI Verios 460 L).

Contact Angle Measurement: Contact angle measurements were conducted with a Ramé-hart goniometer (model 250) at ambient temperature (22–25 °C). A water droplet of 2 μL was carefully deposited onto the sample surface, and the syringe was withdrawn immediately. The water droplet images were captured in five different locations of each sample by a charge-coupled device camera and a 150 W fiber optic illuminator. Finally, the water contact angle was measured using the low-bond axisymmetric drop shape analysis plugin provided by the ImageJ software.[96]

High-Speed Imaging: A Photron SA-X2 high-speed camera was utilized to observe the roll-coating process with a Sigma 1800 mm Macro lens. The images were collected at 200 frames per second (fps). The PDMS ribbing pattern was collected in a high-resolution camera. The collected images were processed by ImageJ software to analyze the wavelength patterns.[97]

Scratch Testing: A Nanovea CB500 mechanical tester was utilized to examine the robustness of the 3.5 wt% CNT-PDMS micropatterned surface. A spherical-shaped indentor (6-mm diameter) was used to scratch the 6–8 mm sample length at 6 mm min^{-1} speed (**Figure 15**). A progressive normal load (F_N) of 1–20 N was applied to the sample at a 19 N min^{-1} loading rate. The machine measured the frictional force (F_{fr}) corresponding to the applied normal force. The frictional coefficient was evaluated as $f = F_N/F_{fr}$. The data were plotted against the scratch length. The first sudden change in the frictional force or coefficient was considered materials' cohesive failure or mode-1 failure (L_{c1}). The second abrupt change in the data is the adhesive failure or mode-2 failure (L_{c2}).[85,86]

Electrical Conductivity Measurement: The samples were prepared in the same method as the surface energy measurement section. After the samples were cured, they were cut into 2.54 mm × 2.54 mm square shapes. The sheet resistivity of the CNT-PDMS composites was measured by the Van der Pauw method by a custom-made four-point probe setup using Keithley 2400 source meter. Four uniform ohmic contacts of copper were placed at the four corners of the samples and connected to the source meter, as shown in Figure 16b. A current
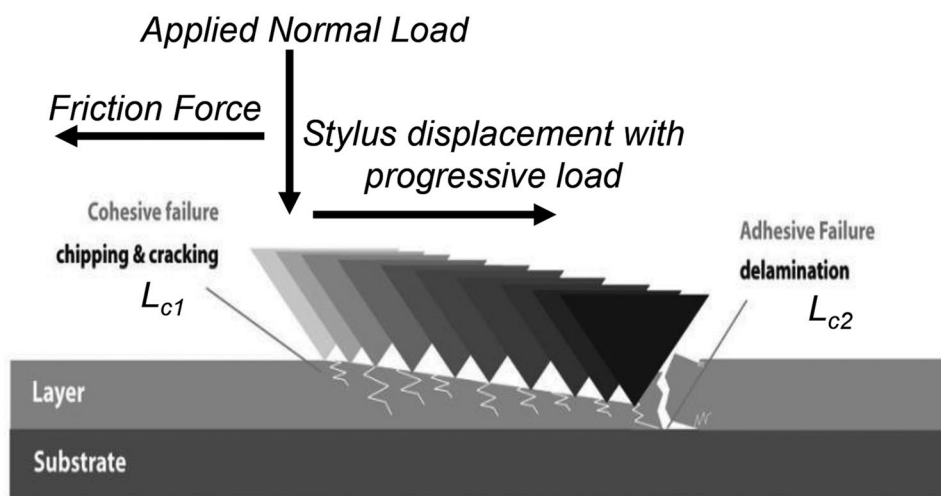

Figure 15. Mechanical scratch testing of the samples showing cohesive and adhesive failure (image reconstructed based on refs. [85,86]).
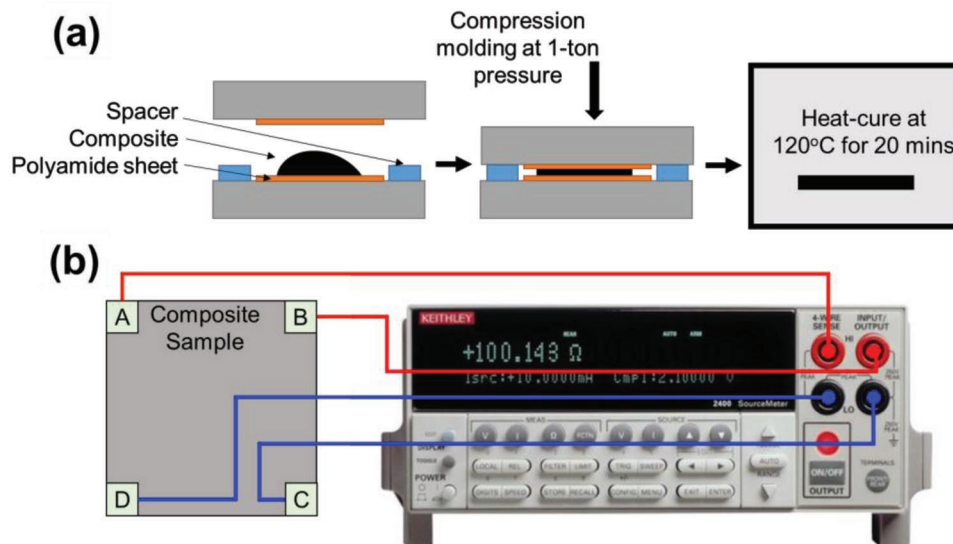
Figure 16. a) Sample preparation of CNT-PDMS composite sample for the electrical measurement. b) Electrical conductivity measurement setup using a custom-made four-point probe following the Van der Pauw method.

was driven along one edge of the sample (e.g., I_{AB}) to make the measurement, and the corresponding voltage on the opposite edge V_{CD} was measured. For this particular case, the ohmic resistance $R_{AB,CD}$ can be calculated based on Ohm's law as follows

$$R_{AB,CD} = \frac{V_{CD}}{I_{AB}} \tag{3}$$

In this method, the resistance was measured both in horizontal and vertical directions by switching the probes, and the average $R_{vertical}$ and $R_{horizontal}$ value was calculated. Next, the sheet resistance R_s of the samples was measured by the Van der Pauw formula as follows

$$e^{-\pi\left(\frac{R_{vertical}}{R_s}\right)} + e^{-\pi\left(\frac{R_{horizontal}}{R_s}\right)} = 1 \tag{4}$$

Statistics: The rheology data reported are mean values over three replicates with yield stress data with SD bar in Figure 1b. The liquid contact angles data to calculate the surface energy was measured in five replicates. The average values and the standard deviation are mentioned in Table S1 (Supporting Information). The CFD simulation data were extracted and analyzed by FLOW-3D Post software. The correlation between PDMS ribbing wavelength, $\lambda_{Ribbing}$ with respect to $\log_{10}(dp/dx)$, $\log_{10}(\dot{\gamma})$, and $\log_{10}(\tau_w)$ was conducted utilizing JMP Pro statistical software. The correlation was validated by a lack of fitting analysis with 95% confidence (p-value > 0.05). The sample's surface roughness data were processed and analyzed by the Multifile Analyzer software. The measured surface data were filtered by the surface shape correction algorithm and next analyzed for wavelength and Wenzel roughness factor. The mean and SD of the data are presented in Table S2 (Supporting Information).

Supporting Information

Supporting Information is available from the Wiley Online Library or from the author.

Acknowledgements

Conflict of Interest

The authors declare no conflict of interest.

Data Availability Statement

The data that support the findings of this study are available from the corresponding author upon reasonable request.

Keywords

[1] X. Wang, B. Ding, J. Yu, M. Wang, *Nano Today* **2011**, *6*, 510.
[2] Z. Guo, W. Liu, B. L. Su, *J. Colloid Interface Sci.* **2011**, *353*, 335.
[3] Q. Xu, W. Zhang, C. Dong, T. S. Sreeprasad, Z. Xia, *J. R. Soc. Interface* **2016**, *13*, 20160300.
[4] W. L. Min, B. Jiang, P. Jiang, *Adv. Mater.* **2008**, *20*, 3914.
[5] C. Peng Guo, Y. Zheng, M. Wen, C. Song, Y. Lin, L. Jiang, P. Guo, Y. Zheng, M. Wen, C. Y. S. Lin, L. Jiang, *Adv. Mater.* **2012**, *24*, 2642.
[6] Q. Li, Z. Guo, *J. Mater. Chem. A* **2018**, *6*, 13549.
[7] L. Li, B. Yan, J. Yang, L. Chen, H. Zeng, L. Li, B. Yan, H. Zeng, J. Yang, L. Chen, *Adv. Mater.* **2015**, *27*, 1294.

[8] J. Yang, X. Zhang, X. Zhang, L. Wang, W. Feng, Q. Li, J. Yang, X. Zhang, L. Wang, W. Feng, X. F. Zhang, Q. Li, *Adv. Mater.* **2021**, *33*, 2004754.

[9] Y. Y. Yan, N. Gao, W. Barthlott, *Adv. Colloid Interface Sci.* **2011**, *169*, 80.

[10] B. Bhushan, *Philos. Trans. R. Soc., A* **2009**, *367*, 1445.

[11] C. Zhang, D. A. Mcadams, J. C. Grunlan, *Adv. Mater.* **2016**, *28*, 8566.

[12] T. Sun, L. Feng, X. Gao, L. Jiang, *Acc. Chem. Res.* **2005**, *38*, 644.

[13] P. Vukusic, J. R. Sambles, *Nature* **2003**, *424*, 852.

[14] M. Srinivasarao, *Chem. Rev.* **1999**, *99*, 1935.

[15] W. Yu, J. Koc, J. A. Finlay, J. L. Clarke, A. S. Clare, A. Rosenhahn, *Biointerphases* **2019**, *14*, 051002.

[16] M. D. Ibrahim, S. N. A. Amran, Y. S. Yunos, M. R. A. Rahman, M. Z. Mohtar, L. K. Wong, A. Zulkharnain, *Appl. Bionics Biomech.* **2018**, *2018*, 7854321.

[17] X. Li, J. Deng, Y. Lu, L. Zhang, J. Sun, F. Wu, *Ceram. Int.* **2019**, *45*, 21759.

[18] G. Liu, Z. Yuan, Z. Qiu, S. Feng, Y. Xie, D. Leng, X. Tian, *Ocean Eng.* **2020**, *199*, 106962.

[19] X. Feng, P. Sun, G. Tian, X. Feng, P. Sun, G. Tian, *Adv. Mater. Interfaces* **2022**, *9*, 2101616.

[20] M. Xu, A. Grabowski, N. Yu, G. Kerezyte, J. W. Lee, B. R. Pfeifer, C.-J. J. Kim, *Phys. Rev. Appl.* **2020**, *13*, 034056.

[21] H. Park, G. Sun, C. J. Kim, *J. Fluid Mech.* **2014**, *747*, 722.

[22] M. Xu, N. Yu, J. Kim, C.-J. Kim, *J. Fluid Mech.* **2021**, *908*, A6.

[23] B. Liu, Y. He, Y. Fan, X. Wang, *Macromol. Rapid Commun.* **2006**, *27*, 1859.

[24] H. S. Hwang, N. H. Kim, S. G. Lee, D. Y. Lee, K. Cho, I. Park, *ACS Appl. Mater. Interfaces* **2011**, *3*, 2179.

[25] S. Kato, A. Sato, *J. Mater. Chem.* **2012**, *22*, 8613.

[26] J. Zou, H. Chen, A. Chunder, Y. Yu, Q. Huo, L. Zhai, *Adv. Mater.* **2008**, *20*, 3337.

[27] S. Lee, J. Lee, J. Park, Y. Choi, K. Yong, *Adv. Mater.* **2012**, *24*, 2418.

[28] L. Zhu, Y. Xiu, J. Xu, P. A. Tamirisa, D. W. Hess, C. P. Wong, *Langmuir* **2005**, *21*, 11208.

[29] X. Hu, L. Chen, T. Ji, Y. Zhang, A. Hu, F. Wu, G. Li, Y. Chen, X. Hu, L. Chen, T. Ji, Y. Zhang, A. Hu, F. Wu, Y. Chen, G. Li, *Adv. Mater. Interfaces* **2015**, *2*, 1500445.

[30] X. Liang, J. Lu, T. Zhao, X. Yu, Q. Jiang, Y. Hu, P. Zhu, R. Sun, C. P. Wong, *Adv. Mater. Interfaces* **2019**, *6*, 1801635.

[31] S. Chae, K. H. Cho, S. Won, A. Yi, J. Choi, H. H. Lee, J. H. Kim, H. J. Kim, *Adv. Mater. Interfaces* **2017**, *4*, 1701099.

[32] M. E. G. Castillo, A. T. Patera, *J. Fluid Mech.* **1997**, *335*, 323.

[33] Y. H. Chong, P. H. Gaskell, N. Kapur, *Chem. Eng. Sci.* **2007**, *62*, 4138.

[34] T. Bauman, T. Sullivan, S. Middleman, *Chem. Eng. Commun.* **1982**, *14*, 35.

[35] J. Greener, T. Sullivan, B. Turner, S. Middleman, *Chem. Eng. Commun.* **1980**, *5*, 73.

[36] G. A. Zevallos, M. S. Carvalho, M. Pasquali, *J. Non-Newtonian Fluid Mech.* **2005**, *130*, 96.

[37] R. J. Fields, M. F. Ashby, *Philos. Mag.* **1976**, *33*, 33.

[38] A. M. Grillet, A. G. Lee, E. S. G. Shaqfeh, *J. Fluid Mech.* **1999**, *399*, 49.

[39] E. Szczurek, M. Dubar, R. Deltombe, A. Dubois, L. Dubar, *J. Mater. Process. Technol.* **2009**, *209*, 3187.

[40] O. Cohu, A. Magnin, *J. Rheol.* **1995**, *39*, 767.

[41] C. K. Yang, D. S. H. Wong, T. J. Liu, *Polym. Eng. Sci.* **2004**, *44*, 1970.

[42] G. P. Bierwagen, *Electrochim. Acta* **1992**, *37*, 1471.

[43] P. Brumm, H. Sauer, E. Dörsam, *Colloids Interfaces* **2019**, *3*, 37.

[44] M. Pudas, J. Hagberg, S. Leppävuori, *Int. J. Electron.* **2005**, *92*, 251.

[45] M. Yamamura, *J. Coat. Technol. Res.* **2020**, *17*, 1447.

[46] J. H. Lee, S. K. Han, J. S. Lee, H. W. Jung, J. C. Hyun, *Korea Aust. Rheol. J.* **2010**, *22*, 75.

[47] M. Rosen, M. Vazquez, *AIP Conf. Proc.* **2007**, *913*, 14.

[48] D. J. Coyle, C. W. Macosko, L. E. Scriven, *J. Rheol.* **1990**, *34*, 615.

[49] F. V. López, L. Pauchard, M. Rosen, M. Rabaud, *J. Non-Newtonian Fluid Mech.* **2002**, *103*, 123.

[50] D. A. Soules, R. H. Fernando, J. E. Glass, *J. Rheol.* **1988**, *32*, 181.

[51] D. J. Coyle, *Liquid Film Coating*, Springer, Netherlands, Dordrecht **1997**, pp. 539–571.

[52] A. Shahsavar, M. Bahiraei, *Powder Technol.* **2017**, *318*, 441.

[53] S. Abbasi, S. M. Zebarjad, S. H. N. Baghban, A. Youssefi, M.-S. Ekrami-Kakhki, *J. Therm. Anal. Calorim.* **2016**, *123*, 81.

[54] B. Jo, D. Banerjee, *Mater. Lett.* **2014**, *122*, 212.

[55] S. Mueller, E. W. Llewellin, H. M. Mader, *Proc. R. Soc. A: Math. Phys. Eng. Sci.* **2010**, *466*, 1201.

[56] E. Anczurowski, S. G. Mason, *Trans. Soc. Rheol.* **1968**, *12*, 209.

[57] C. W. Macosko, *Rheology: Principles, Measurements, and Applications*, VCH, Weinheim **1994**.

[58] R. D. Corder, P. Adhikari, M. C. Burroughs, O. J. Rojas, S. A. Khan, *Soft Matter* **2020**, *16*, 8602.

[59] S. A. Jin, E. G. Facchine, S. A. Khan, O. J. Rojas, R. J. Spontak, *J. Colloid Interface Sci.* **2021**, *599*, 207.

[60] S. Wang, H. Tang, J. Guo, K. Wang, *Carbohydr. Polym.* **2016**, *147*, 455.

[61] M. Razavi-Nouri, A. Sabet, M. Mohebbi, *Polym. Bull.* **2020**, *77*, 5933.

[62] T. V. Neumann, E. G. Facchine, B. Leonardo, S. Khan, M. D. Dickey, *Soft Matter* **2020**, *16*, 6608.

[63] Y. Y. Huang, S. V. Ahir, E. M. Terentjev, *Phys. Rev. B: Condens. Matter Mater. Phys.* **2006**, *73*, 125422.

[64] N. A. Burns, M. A. Naclerio, S. A. Khan, A. Shojaei, S. R. Raghavan, *J. Rheol.* **2014**, *58*, 1599.

[65] S. Wu, *J. Polym. Sci., Part C: Polym. Symp.* **1971**, *34*, 19.

[66] J. E. Mark, *Physical Properties of Polymers Handbook*, 2nd ed., Springer, Berlin **2007**.

[67] B. B. Sauer, N. V. Dipaolo, *J. Colloid Interface Sci.* **1991**, *144*, 527.

[68] M. Morra, E. Occhiello, R. Marola, F. Garbassi, P. Humphrey, D. Johnson, *J. Colloid Interface Sci.* **1990**, *137*, 11.

[69] A. Dresel, U. Teipel, *Colloids Surf., A* **2016**, *489*, 57.

[70] S. C. Roh, E. Y. Choi, Y. S. Choi, C. K. Kim, *Polymer* **2014**, *55*, 1527.

[71] S. Nuriel, L. Liu, A. H. Barber, H. D. Wagner, *Chem. Phys. Lett.* **2005**, *404*, 263.

[72] Y. C. Jeong, S. J. Yang, K. Lee, A.-Y. Kamebuchi, Y. Kamimoto, M. H. Al-Saleh, *Mater. Res. Express* **2019**, *6*, 115088.

[73] S.-H. Park, S. Lee, D. Moreira, P. R. Bandaru, I. Han, D.-J. Yun, *Sci. Rep.* **2015**, *5*, 15430.

[74] D. J. Coyle, C. W. Macosko, L. E. Scriven, *J. Fluid Mech.* **1986**, *171*, 183.

[75] D. J. Coyle, C. W. Macosko, L. E. Scriven, *AIChE J.* **1987**, *33*, 741.

[76] M. S. Owens, M. Vinjamur, L. E. Scriven, C. W. Macosko, *J. Non-Newtonian Fluid Mech.* **2011**, *166*, 1123.

[77] C. Lee, C. H. Choi, C. J. Kim, *Exp. Fluids* **2016**, *57*, 176.

[78] M. P. Schultz, *Biofouling* **2007**, *23*, 331.

[79] Y. Xia, P. Cai, Y. Liu, J. Zhu, R. Guo, W. Zhang, Y. Gan, H. Huang, J. Zhang, C. Liang, X. He, Z. Xiao, *J. Electron. Mater.* **2021**, *50*, 3084.

[80] B. Earp, J. Simpson, J. Phillips, D. Grbovic, S. Vidmar, J. McCarthy, C. C. Luhrs, *Nanomaterials* **2019**, *9*, 491.

[81] D. M. Kalyon, E. Birinci, R. Yazici, B. Karuv, S. Walsh, *Polym. Eng. Sci.* **2002**, *42*, 1609.

[82] A. Mora, P. Verma, S. Kumar, *Composites, Part B* **2020**, *183*, 107600.

[83] C. Lee, C. J. Kim, *Phys. Rev. Lett.* **2011**, *106*, 014502.

[84] M. Xu, C. T. Liu, C. J. Kim, *Langmuir* **2020**, *36*, 8193.

[85] D. Li, *Scratch Hardness Measurement Using Tribometer*, Nanovea, Irvine, CA **2014**.

[86] D. Li, *Understanding Coating Failures Using Scratch Testing*, Nanovea, Irvine, CA **2013**.

[87] X. Li, J. Deng, H. Yue, D. Ge, X. Zou, *Tribol. Int.* **2019**, *134*, 240.

[88] S. N. Li, Z. R. Yu, B. F. Guo, K. Y. Guo, Y. Li, L. X. Gong, L. Zhao, J. Bae, L. C. Tang, *Nano Energy* **2021**, *90*, 106502.

[89] S. W. Dai, Y. L. Gu, L. Zhao, W. Zhang, C. H. Gao, Y. X. Wu, S. C. Shen, C. Zhang, T. T. Kong, Y. T. Li, L. X. Gong, G. D. Zhang, L. C. Tang, *Composites, Part B* **2021**, *225*, 109243.

[90] Y. T. Li, W. J. Liu, F. X. Shen, G. D. Zhang, L. X. Gong, L. Zhao, P. Song, J. F. Gao, L. C. Tang, *Composites, Part B* **2022**, *238*, 109907.

[91] H. J. Walls, S. B. Caines, A. M. Sanchez, S. A. Khan, *J. Rheol.* **2003**, *47*, 847.

[92] F. M. Fowkes, *J. Phys. Chem.* **1963**, *67*, 2538.

[93] D. K. Owens, R. C. Wendt, *J. Appl. Polym. Sci.* **1969**, *13*, 1741.

[94] N. Selvakumar, H. C. Barshilia, K. S. Rajam, *J. Appl. Phys.* **2010**, *108*, 013505.

[95] A. Kozbial, Z. Li, C. Conaway, R. McGinley, S. Dhingra, V. Vahdat, F. Zhou, B. Durso, H. Liu, L. Li, *Langmuir* **2014**, *30*, 8598.

[96] A. F. Stalder, G. Kulik, D. Sage, L. Barbieri, P. Hoffmann, *Colloids Surf., A* **2006**, *286*, 92.

[97] C. A. Schneider, W. S. Rasband, K. W. Eliceiri, *Nat. Methods* **2012**, *9*, 671.

ADVANCED MATERIALS INTERFACES

Supporting Information

Template-Free Scalable Fabrication of Linearly Periodic Microstructures by Controlling Ribbing Defects Phenomenon in Forward Roll Coating for Multifunctional Applications

Md Didarul Islam, Himendra Perera, Benjamin Black, Matthew Phillips, Muh-Jang Chen, Greyson Hodges, Allyce Jackman, Yuxuan Liu, Chang-Jin Kim, Mohammed Zikry, Saad Khan, Yong Zhu, Mark Pankow, and Jong Eun Ryu*

Supporting Information

Template-free scalable fabrication of linearly periodic microstructures by controlling ribbing defects phenomenon in forward roll coating for multifunctional applications

Md Didarul Islam, Himendra Perera, Benjamin Black, Matthew Phillips, Muh-Jang Chen, Greyson Hodges, Allyce Jackman, Yuxuan Liu, Chang-Jin Kim, Mohammed Zikry, Saad Khan, Yong Zhu, Mark Pankow, Jong Eun Ryu[*]*
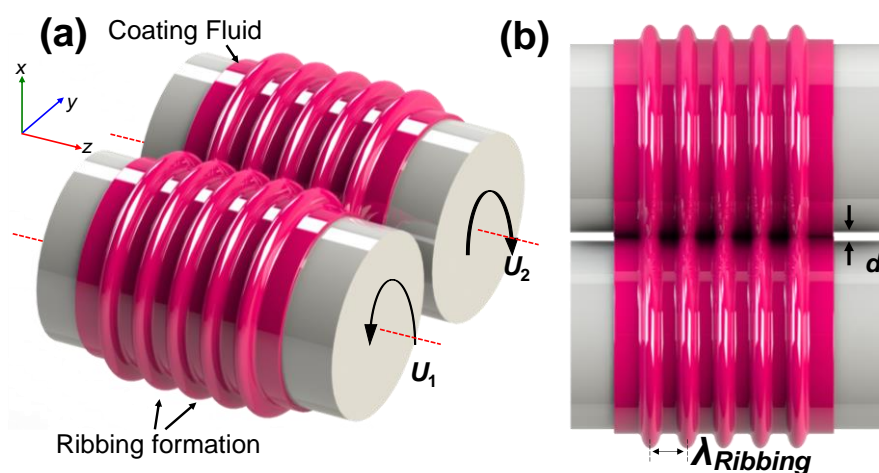
Corresponding Author*

Figure S1. (a-b) Schematic of the ribbing formation phenomenon on a two-roll coater.
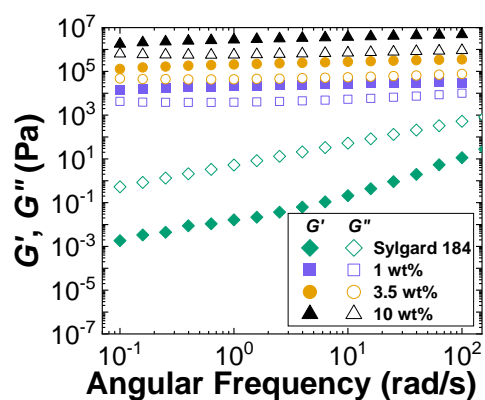
Figure S2. Elastic (G') and viscous (G'') modulus as a function of angular frequency.
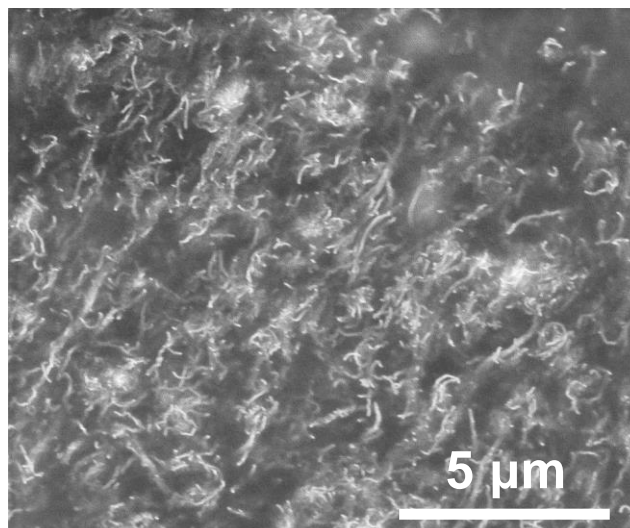
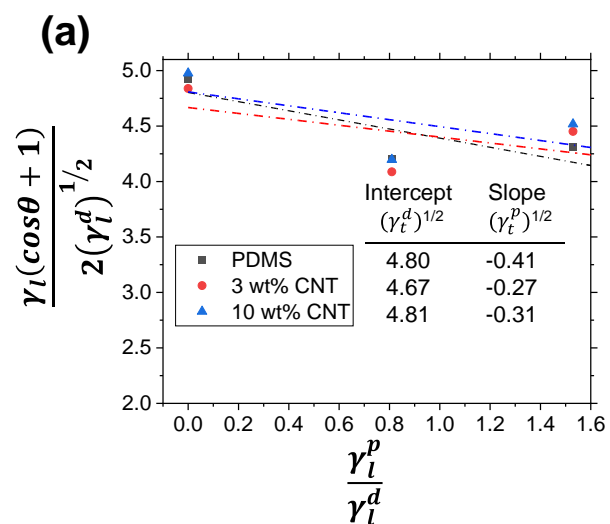**Figure S3.** CNTs distribution in PDMS matrix.

Figure S4. The measured liquid contact angles were fitted in the Owens-Wendt model to evaluate the apparent surface energy.
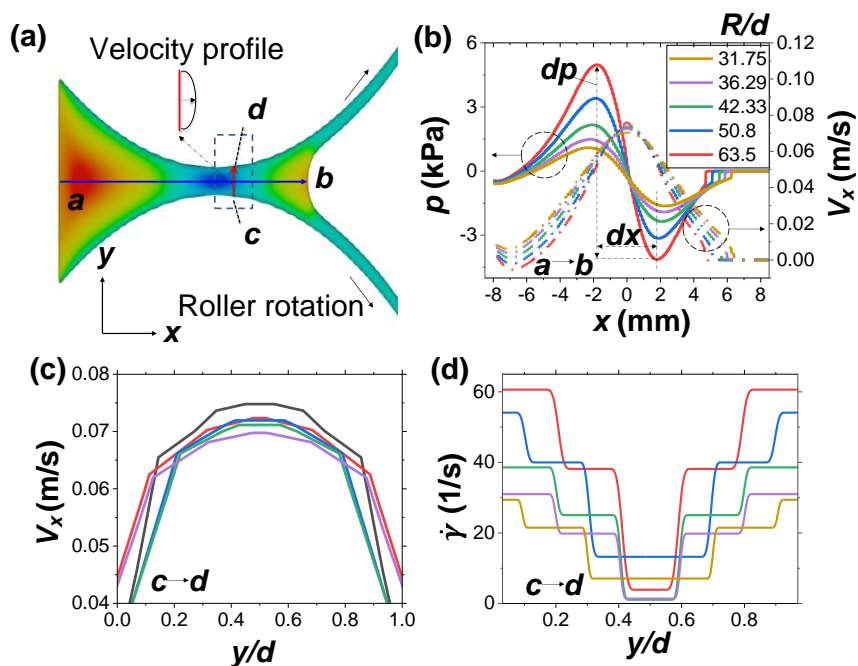
Figure S5. (a) Cross-section of the fluid profile showing the velocity and pressure gradient. (b) Absolute pressure, p and fluid velocity, V_x at the direction of fluid flow (*a-b* direction) for R/d = 31.75, 36.29, 42.33, 50.8, 63.5 at a roller speed of 10 rpm. (c) The fluid velocity profile, V_x, in the *c-d* direction. (d) Shear rate ($\dot{\gamma}$) generated due to the velocity gradient in the *c-d* direction.
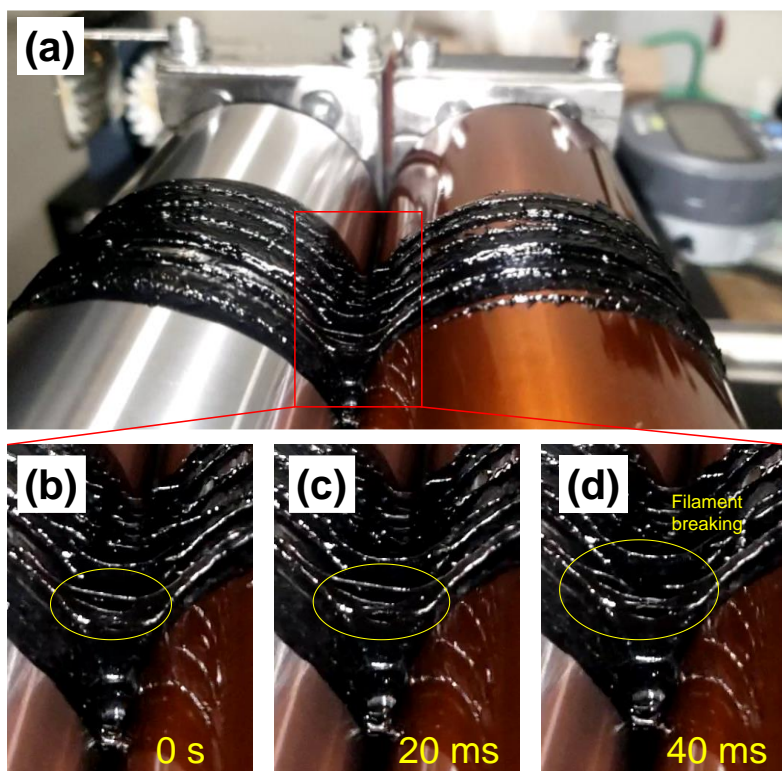

Figure S6. (a) Filamentation phenomenon on 0.5 wt% CNT-PDMS composite roll-coating (b) Filament initiation, (c) Filament elongation, (d) Filament breakage.
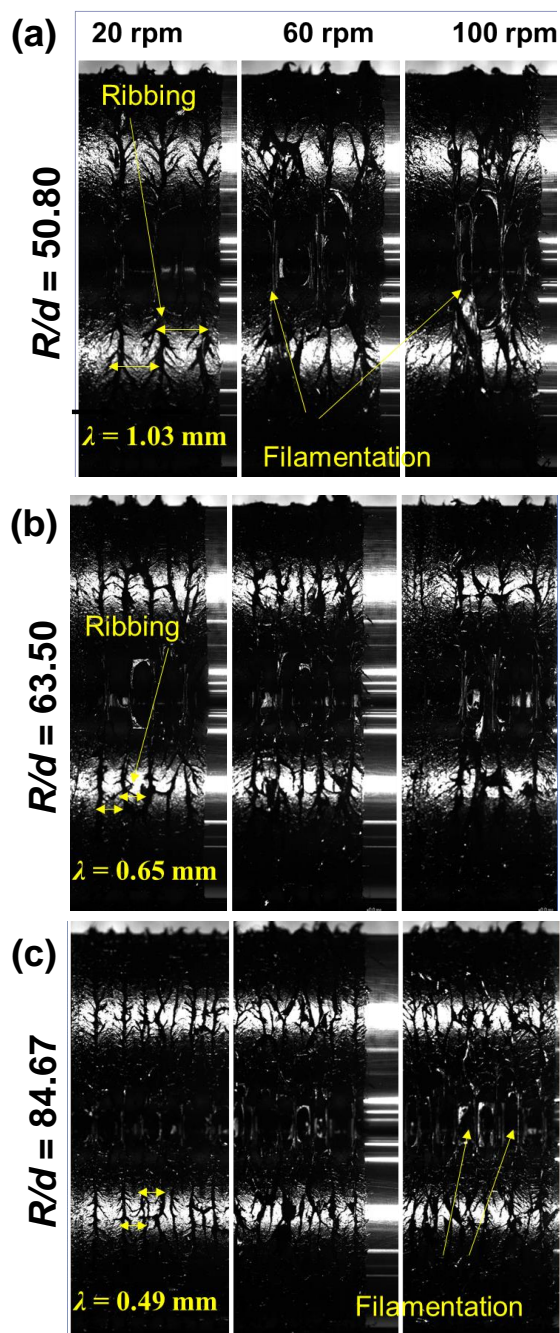
3

Figure S7. High-speed images were captured for roll coating of 1wt% CNT-PDMS for various roll-coating speeds of 20 rpm, 60 rpm, and 100 rpm for *R/d* of (a) 50.80, (b) 63.5, and (c) 84.67. The ribbing was relatively stable at a lower speed, whereas the higher speed incurred more filamentation and tip-splitting.
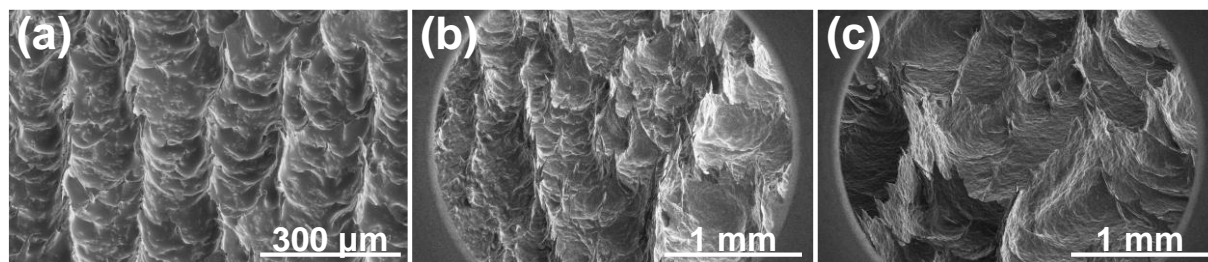
Figure S8. SEM images of 3 wt% CNT-PDMS samples at 50 rpm speed, and (a) $R/d = 63.5$; (b) $R/d = 84.67$; (c) $R/d = 101.6$.

Table S1. Surface energy measurement based on the Owens-Wendt model

Material	Test liquid	Liquid contact angle, θ		$\dfrac{\gamma_l^p}{\gamma_l^d}$	$\dfrac{\gamma_l(cos\theta + 1)}{2(\gamma_l^d)^{1/2}}$	γ_t^d (mJ m^{-2})	γ_t^p (mJ m^{-2})	$\gamma_t = \gamma_t^p + \gamma_t^d$ (mJ m^{-2})
		Mean	SD					
PDMS	DIM	67.48	1.27	0.00	4.93			
	EG	93.28	0.81	0.81	4.20	23.06	0.17	23.23
	Water	116.52	0.53	1.53	4.32			
3% CNT	DIM	69.04	1.47	0.00	4.84			
	EG	94.75	1.09	0.81	4.09	21.78	0.07	21.85
	Water	115.40	1.78	1.53	4.45			
10% CNT	DIM	66.65	0.98	0.00	4.98			
	EG	93.33	0.24	0.81	4.20	23.12	0.10	23.22
	Water	114.87	1.64	1.53	4.52			

Table S2. Sample roughness measurement

R/d	$\lambda_{Ribbing}$ (µm)		$\lambda_{Filamentation}$ (µm)		r	WCA	
	Mean	SD	Mean	SD		Mean	SD
56.44	777.92	89.8	455.23	186.5	1.597	128.17	7.55
63.5	618.21	146.55	337.38	82.03	2.01	133.64	7.09
72.57	148.50	17.58	200.63	40.9	2.497	136.98	7.54
84.67	114.34	12.68	146.93	27.8	2.44	137.274	3.81
101.6	224.18	30.68	230.07	68.4	3.55	150.63	4.08
127	199.41	24.26	242.98	49.03	3.5	158.13	5.47